A&A 398, 901–918 (2003)
DOI: 10.1051/0004-6361:20021721


Astronomy & Astrophysics

# A deep VLA survey at 6 cm in the Lockman Hole

P. Ciliegi[1], G. Zamorani[1,2], G. Hasinger[3,4], I. Lehmann[3,4], G. Szokoly[3,4], and G. Wilson[5,6]

[1] INAF: Osservatorio Astronomico di Bologna, via Ranzani 1, 40127 Bologna, Italy
[2] Istituto di Radioastronomia, CNR, via Gobetti 101, 40129 Bologna, Italy
[3] Astrophysikalisches Institute Postdam, An der Sternwarte 16, 14482, Postdam, Germany
[4] Max-Planck-Institut für extraterrestrische Physik Giessenbachstraße, 85748 Garching, Germany
[5] Brown University, Physics Department, Providence, RI 02912, USA
[6] SIRTF Science Center, California Institute of Technology, Mail Code 220-6, 1200 East California Boulevard, Pasadena, CA 91125, USA

Received 7 May 2002 / Accepted 18 November 2002

**Abstract.** We have obtained a deep radio image with the Very Large Array at 6 cm in the Lockman Hole. The noise level in the central part of the field is ∼11 $\mu$Jy. From these data we have extracted a catalogue of 63 radio sources with a maximum distance of 10 arcmin from the field center and with peak flux density greater than 4.5 times the local rms noise. The di fferential source counts are in good agreement with those obtained by other surveys. The analysis of the radio spectral index suggests a flattening of the average radio spectra and an increase of the population of flat spectrum radio sources in the faintest flux bin. Cross correlation with the ROSAT/XMM X-ray sources list yields 13 reliable radio/X-ray associations, corresponding to ∼21% of the radio sample. Most of these associations (8 out of 13) are classified as type II AGN.
Using optical CCD ($V$ and $I$) and $K'$ band data with approximate limits of $V \sim 25.5$ mag, $I \sim 24.5$ mag and $K' \sim 20.2$ mag, we found an optical identification for 58 of the 63 radio sources. This corresponds to an identification rate of ∼92%, one of the highest percentages so far available. From the analysis of the colour-colour diagram and of the radio flux – optical magnitude diagram we have been able to select a subsample of radio sources whose optical counterparts are likely to be high redshift ($z > 0.5$) early-type galaxies, hosting an Active Galactic Nucleus responsible of the radio activity. This class of objects, rather than a population of star-forming galaxies, appears to be the dominant population ($\gtrsim$50%) in a 5 GHz selected sample with a flux limit as low as 50 $\mu$Jy.
We also find evidence that at these faint radio limits a large fraction (∼60%) of the faintest optical counterparts (i.e. sources in the magnitude range $22.5 < I < 24.5$ mag) of the radio sources are Extremely Red Objects (EROs) with $I - K' > 4$ and combining our radio data with existing ISO data we conclude that these EROs sources are probably associated with high redshift, passively evolving elliptical galaxies. The six radio selected EROs represent only ∼2% of the optically selected EROs present in the field. If their luminosity is indeed a sign of AGN activity, the small number of radio detections suggests that a small fraction of the EROS population contains an active nucleus.

**Key words.** cosmology: observations – galaxies: general: starburst – quasar: general

## 1. Introduction

Deep radio surveys reaching flux density of few $\mu$Jy have revealed a population of faint sources in excess with respect to the "normal" population of powerful radio galaxies. While the radio source counts above a few mJy are fully explained in terms of a population of classical radio sources powered by active galactic nuclei (AGN) and hosted by elliptical galaxies, below this flux starts to appear a population of star-forming galaxies similar to the nearby starburst population dominating the *Infrared Astronomical Satellite* (IRAS) 60 $\mu$m counts. The excellent correlation between radio and mid–infrared emission for these objects (Condon 1992; Yun et al. 2001) suggests that indeed the radio emission in these galaxies is directly related to the amount of star formation. For this reason, faint radio surveys and identification of the optical counterparts can in principle be used, together with optical and infrared surveys, to study the evolution of the star formation history. This would require a clear understanding of the flux level at which the star–forming galaxies do indeed become the dominant population of faint radio sources. However, despite many dedicated efforts (see, for example, Benn et al. 1993; Hammer et al. 1995; Gruppioni et al. 1999; Georgakakis et al. 1999; Prandoni et al. 2001) the relative fractions of the populations responsible of the sub-mJy radio counts (AGN, starburst, late and early type galaxies), are still far from being well established.

Optical spectroscopy for a complete sample of faint radio sources would be the most direct way for a proper classification of the optical counterparts. However, the very faint magnitudes

*Send offprint requests to*: P. Ciliegi, e-mail: ciliegi@bo.astro.it

of a significant fraction of the objects associated to faint radio sources makes this approach difficult even for 8 m–class telescopes. Alternatively, approximate classification of the counterparts can be achieved using photometric (colours) and radio (spectral index) data.

The purpose of this work is to shed some light into the nature of these sources by studying a new faint radio sample for which we have analyzed the radio spectral properties and derived photometric optical identifications down to faint optical and $K$ band magnitudes. To further strengthen these goals, we have observed a region of the sky at 6 cm centered in the Lockman Hole, where excellent data are already available at 20 cm (de Ruiter et al. 1997), in the far-infrared band (Fadda et al. 2002; Rodighiero et al. in preparation), in the near infrared and optical bands (Schmidt et al. 1998; Lehmann et al. 2000; Lehmann et al. 2001; Wilson et al. 2001) and in the X-ray band (Hasinger et al. 2001). In Sect. 2 we give a general description of the radio observations, while the radio catalogue and the source counts are presented in Sect. 3. In Sect. 4 we present the associations of the 6 cm sources with the radio (20 cm), near–infrared, optical, and X-ray sources. Finally, Sect. 5 is devoted to the discussion of our results, while Sect. 6 summarizes our conclusions.

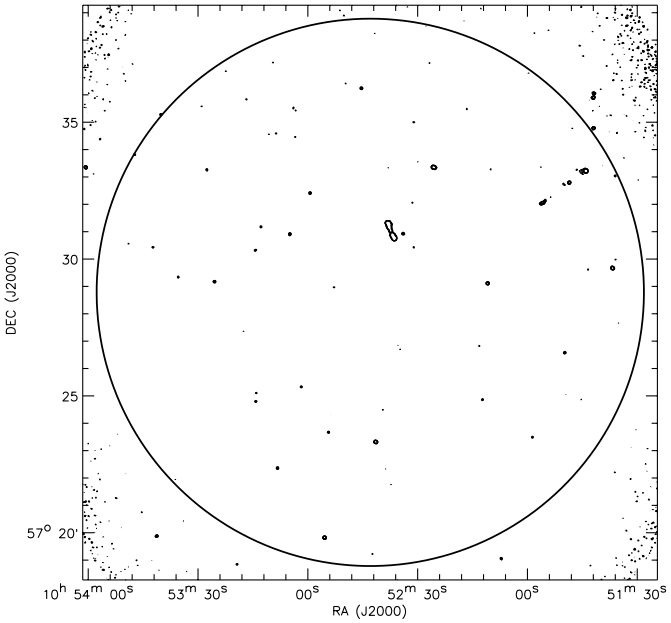


**Fig. 1.** Contour plot of the 6 cm VLA image of the Lockman Hole. Contours are drawn starting from 4.5 times the local rms noise (see Fig. 2) with an increasing factor of $\sqrt{2}$. The circle of 10 arcmin radius shows the area used to extract the sources.

## 2. The radio observations and data reduction

The VLA observations were done in three runs of eleven hours each on January 16, 17 and 19, 1999 at 4835 and 4885 MHz with a bandwidth of 50 MHz in C configuration. A total of seven pointings in a hexagonal grid with a size of $\theta_{\rm FWHP}/\sqrt{2} \sim$ 6.4 arcmin (where $\theta_{\rm FWHP}$ is the full-width at half-power of the primary beam, 9 arcmin at 5 GHz) plus one at the center were observed for 4 hours each around the ROSAT ultra-deep *HRI* field center RA(2000) = $10^{\rm h}52^{\rm m}43^{\rm s}$, Dec(2000) = $57°28'48''$. This choice of pointing positions was adopted in order to obtain a reasonably uniform rms noise level in the inner part of the ROSAT ultra deep *HRI* field.

All the data were analyzed using the NRAO AIPS reduction package. The data were calibrated using 3C 286 as primary flux density calibrator (assuming a flux density of 7.5103 Jy at 4835 MHz and 7.4617 Jy at 4885 MHz) and the source 1035+564 as a phase and secondary amplitude calibrator.

For each of the seven fields we constructed an image of $1024 \times 1024$ pixels, with a pixel-size of 1.0 arcsec. Each observation was cleaned using the task IMAGR, using a restoring beam of $4 \times 4$ arcsec. The rms noise levels in the cleaned (not primary beam corrected) images are uniform and of the order of 11 $\mu$Jy. Finally, using the AIPS task LGEOM, HGEOM and LTESS, we have combined all the seven pointings, creating a single mosaic map of $2048 \times 2048$ pixels. Contour plot of the mosaic map is shown in Fig. 1.

As expected, the mosaic map has a regular noise distribution: a circular central region with a flat noise distribution, surrounded by an outer region where the noise increases for increasing distance from the center. No structures or irregularities were found in the rms noise map. The rms values as a function of the distance from the field center are well fitted by the function: $\mathrm{rms}(\theta_{\rm off}) = 8.2 \times 10^{-5} \times \theta_{\rm off}^{5.05} + 11$ $\mu$Jy where $\theta_{\rm off}$ is the off-axis angle in arcmin. Measurements of the rms noise at various distances from the field center and the fitting function are shown in Fig. 2.

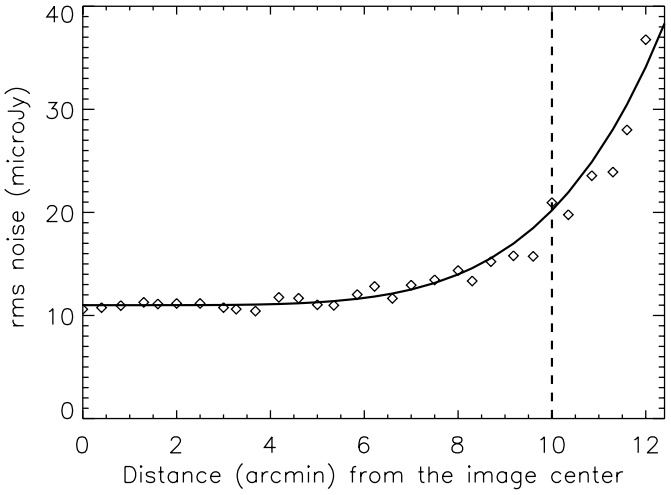


**Fig. 2.** The rms noise (in $\mu$Jy) as a function of the distance from the image center. The solid line is the best fit function rms = $8.2 \times 10^{-5} \times \theta_{\rm off}^{5.05} + 11$ $\mu$Jy. The dashed vertical line indicates the maximum distance from the center within which the sample described in this paper has been extracted.

Given the rapid increase of the rms noise at large off-axis angles, we have limited the extraction of the sources to an area with $\theta_{\rm off} \leq 10$ arcmin, corresponding to 0.087 square degree.

## 3. The source catalogue

### 3.1. Source detection

The criterion we adopted for including a source in the catalogue is that its peak flux density, $S_P$, is ≥4.5 times the average rms value at the off-axis angle of the source (see Fig. 2). In order to choose the threshold in $S_P$ we analyzed the map with the negative peaks using different threshold values (3.5, 4.0, 4.5, 5.0, 5.5 and 6 respectively). The choice of 4.5 as threshold in $S_P$ is a compromise between a low flux limit and the necessity to keep the number of spurious sources as low as possible. From the analysis of the negative peaks, we are confident that at most three or four spurious sources are present in the sample.

The sources were extracted using the task SAD (Search And Destroy) which selects all the sources with peaks brighter than a given level. For each selected source the flux, the position and the size are estimated using a least square Gaussian fit. However the Gaussian fit may be unreliable both for faint and bright sources. In fact the noise map could influence the fit for faint sources (Condon 1997), while the differences between the Gaussian beam and the real synthesized beam could in principle influence the goodness of a Gaussian fit even for sources with a large signal to noise ratio (Windhorst et al. 1984). Thus, we used SAD to extract all the sources whose peak flux $S_P$ was greater than 3 times the local rms value. Subsequently, we derived the peak flux for all the sources using a second degree interpolation (task MAXFIT). Only the sources with a MAXFIT peak flux density ≥4.5 $\sigma$ were included in the final sample. Hereafter we will use the MAXFIT peak flux density as the peak flux density $S_P$ of the sources. For irregular and extended sources the total flux density was determined by summing the values of all the pixels covering the source.

With this procedure we selected 63 radio sources (2 of which have multiple components for a total of 68 components) over a total area of 0.087 deg$^2$.

In Fig. 3 we plot the ratio between the total ($S_T$) and peak flux density ($S_P$) as a function of the peak flux density for all the radio sources. Since the ratio of the total flux to the peak flux is a direct measure of the extension of a radio source, it can be used to discriminate between resolved or extended sources (i.e. larger than the beam) and unresolved sources. To select the extended sources, we have determined the lower envelope of the flux ratio distribution of Fig. 3 and we have mirrored it above the $S_T/S_P = 1$ value (upper envelope of Fig. 3). We have considered extended the 12 sources laying above the upper envelope that can be characterized by log $(S_T/S_P) = -\log(1-0.15 / S_P^{0.3})$. However we should note that only 5 of the 12 sources classified as extended lie significantly above the upper envelope (see Fig. 3) and can be assumed as "genuine" extended sources. The other 7 sources just above the upper envelope might also be unresolved sources whose total flux has been overestimated due to the noise effect (see Windhorst et al. 1984 for a detailed discussion). Throughout the paper we have used the integrated flux for the 12 formally extended sources and the peak flux for the unresolved sources in all the calculations involving the radio flux.

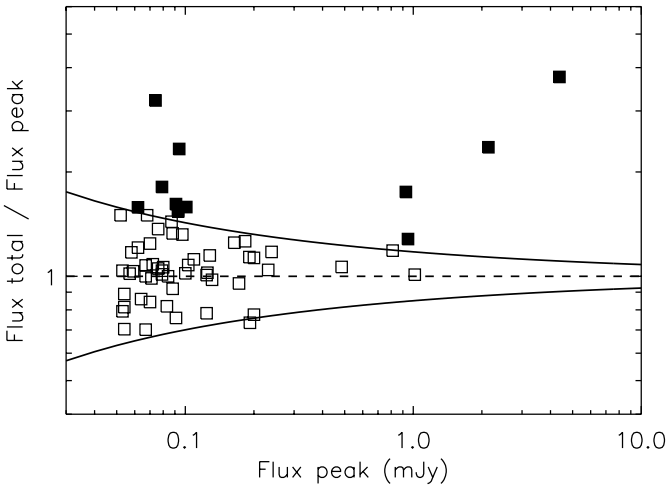


**Fig. 3.** Ratio of the total flux, $S_T$, to the peak flux, $S_P$, as a function of the peak flux $S_P$ for all the 6 cm radio sources in the Lockman Hole. The solid lines show the upper and lower envelopes of the flux ratio distribution containing all the sources considered unresolved (open squares). Filled squares show extended sources.

The catalogue with the 63 sources (68 components) is given in Table 1. For each source we report the name, the peak flux density $S_P$ (and relative error $\sigma_{S_P}$) in mJy, the total flux density $S_T$ in mJy and error, the RA and Dec (J2000) and corresponding errors. Moreover, for resolved sources we also report the full width half maximum (*FWHM*) of the non deconvolved major and minor axes ($\theta_M$ and $\theta_m$ in arcsec) and the position angle PA of the major axis (in degrees, measured east to north).

All the errors in the source parameters were determined following the recipes given by Condon (1997). Also in the calculation of the flux error we used the integrated flux for extended sources and the peak flux for unresolved sources. For the latter sources we used $\theta_M = \theta_m = FWHM$ of synthesized beam =4 arcsec.

The different components of multiple sources are labeled "A", "B", etc., followed by a line labeled "T" in which flux and position for the total sources are given. Fig. 4 illustrates the distributions of peak flux densities for the 63 sources in the catalogue.

### 3.2. Position errors

The projection of the major and minor axis errors onto the right ascension and declination axes produces the total rms position errors given by Condon et al. (1998)

$$\sigma_\alpha^2 = \varepsilon_\alpha^2 + \sigma_{x_0}^2 \sin^2(\mathrm{PA}) + \sigma_{y_0}^2 \cos^2(\mathrm{PA}) \quad (1)$$

$$\sigma_\delta^2 = \varepsilon_\delta^2 + \sigma_{x_0}^2 \cos^2(\mathrm{PA}) + \sigma_{y_0}^2 \sin^2(\mathrm{PA}) \quad (2)$$

where $(\varepsilon_\alpha, \varepsilon_\delta)$ are the "calibration" errors, $\sigma_{x_0}^2 = \theta_M^2/(4\ln 2)\rho^2$, $\sigma_{y_0}^2 = \theta_m^2/(4\ln 2)\rho^2$ with $\rho$ the effective signal to noise ratio as defined in Condon (1997).

The mean image offset $< \Delta\alpha >$, $< \Delta\delta >$ (defined as radio minus optical position) and rms calibration uncertainties $\varepsilon_\alpha^2$ and $\varepsilon_\delta^2$ are best determined by comparison with accurate positions of sources strong enough that the noise plus

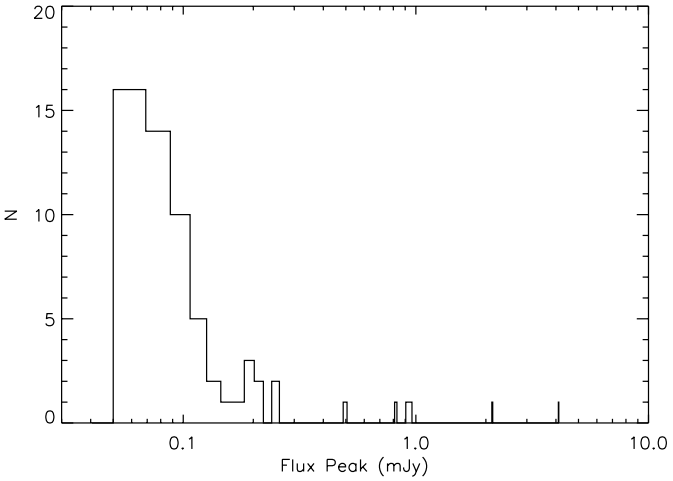


**Fig. 4.** Distribution of peak flux densities for 6 cm radio sources in the Lockman Hole.

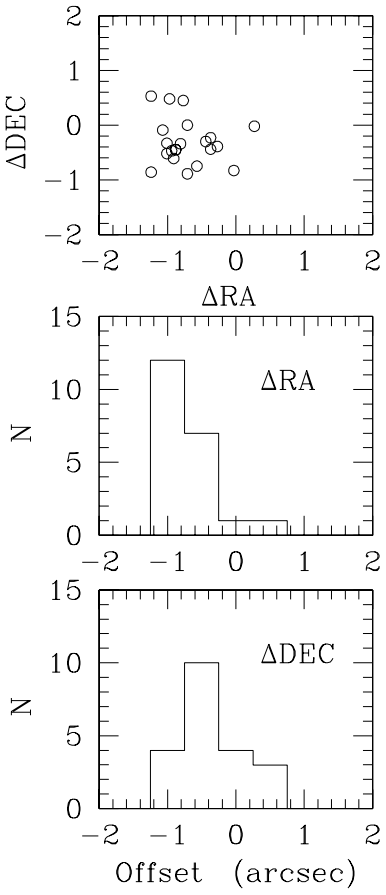


**Fig. 5.** Position offset for strong point sources (20 sources in our survey detected with $S_P > 6\sigma$ and with a point like-optical counterpart in the $V$ band CCD).

confusion terms are much smaller than the calibration terms. We used the 6 cm positions of 20 strong compact sources (detected with $S_P > 6\sigma$) identified with point like optical counterparts in the $V$ band CCD (i.e. we excluded the sources that have an extended or a multiple optical counterparts). Their offsets $\Delta\alpha$ and $\Delta\delta$ are shown in Fig. 5. The mean offsets are $< \Delta\alpha >= -0.71 \pm 0.09''$ and $< \Delta\delta >= -0.31 \pm 0.09''$. These offsets have not been applied to the radio positions reported in Table 1, but they should be removed (adding $0.71''$ in RA and $0.31''$ in Dec at the radio position) to obtain the radio position in the same reference frame as the optical CCD.

From the distributions of $\Delta\alpha$ and $\Delta\delta$ shown in Fig. 5 we have estimated the rms calibration errors: $\varepsilon_\alpha = 0.36''$ and $\varepsilon_\delta = 0.43''$. Since the 20 objects used for this derivation are scattered over the entire field of view, the small values of $\varepsilon_\alpha$ and $\varepsilon_\delta$ show that our mosaic maps are not affected by relevant geometric distortions induced by the approximation of a finite portion of the spherical sky with a bi-dimensional plane (see Perley 1989; Condon et al. 1998). Using these calibration errors, positional uncertainties for all sources have been calculated according to Eqs. (1) and (2). The rms position uncertainties ($\sigma_\alpha$, $\sigma_\delta$) of all the sources in our catalogue are reported in Table 1 (see Cols. 8 and 9) and plotted as a function of peak flux in Fig. 6.

### *3.3. Survey completeness and source counts*

The sample of 63 sources listed in Table 1 has been used to construct the source counts distributions. The rms noise as a function of distance from the center (Fig. 2) was used to obtain the detectability area as a function of flux density. In Fig. 7 the solid angle over which a source with a peak flux density $S_P$ can be detected is plotted as a function of flux density.

The two sources with multiple components have been treated as a single radio source. In computing the counts we have used the integrated flux for extended sources and the peak flux for unresolved sources (see Sect. 3.1 for the definition of resolved and unresolved sources).

#### 3.3.1. Completeness

Before discussing the source counts (see next section) we describe here the simulations that we performed in order to estimate the combined effect of noise, source extraction technique and resolution bias on the completeness of our sample. We constructed a simulated sample of radio sources down to a flux level of 0.025 mJy with a density in the sky given by $N(>S) = 0.42 \times (S/30)^{-1.18}$ (where $N(>S)$ is the number of sources (arcmin)$^{-2}$ with total flux greater than $S$ in $\mu$Jy, Fomalont et al. 1991) and an appropriate angular size distribution. Using the relation reported by Windhorst et al. (1990) between the median angular size ($\theta_{\rm med}$) and the radio flux $\theta_{\rm med} = 2'' \, S^{0.30}_{1.4\ {\rm GHz}}$ we estimated a median angular size between $0.95''$ and $1.54''$ in the flux interval $S_{5\ {\rm GHz}} = 0.05$–$0.25$ mJy where we have ~90% of our sources (56/63). The 5 GHz flux density of our survey were transformed to 1.4 GHz using a radio spectral index $\alpha_r = 0.4$. Following Windhorst et al. (1990) we have assumed $h(\theta) = \exp(-\ln 2(\theta/\theta_{\rm med})^{0.62})$ for the integral angular distribution. We injected the sources simulated with the above recipes (each of them with known flux density and size) in the CLEANed sky images of the field. Then these sources were recovered from the image using the same procedure adopted to extract the real sources (see Sect. 3.1) and binned in flux intervals. We repeated this simulation five times. From the

**Table 1.** The 4.5$\sigma$ radio sample.

| Name | $S_P$ (mJy) | $\sigma_{S_P}$ (mJy) | $S_T$ (mJy) | $\sigma_{S_T}$ (mJy) | RA (J2000) | Dec (J2000) | $\sigma_\alpha$ ($''$) | $\sigma_\delta$ ($''$) | $\theta_M$ ($''$) | $\theta_m$ ($''$) | PA deg |
|---|---|---|---|---|---|---|---|---|---|---|---|
| LOCK_6 cm_J105135+572739 | 0.079 | 0.017 | 0.079 | 0.017 | 10 51 35.42 | 57 27 39.6 | 0.59 | 0.51 | 0.0 | 0.0 | 0.0 |
| LOCK_6 cm_J105136+572959 | 0.087 | 0.017 | 0.087 | 0.017 | 10 51 36.19 | 57 29 59.1 | 0.89 | 0.51 | 0.0 | 0.0 | 0.0 |
| LOCK_6 cm_J105136+573302 | 0.200 | 0.020 | 0.200 | 0.020 | 10 51 36.24 | 57 33 2.6 | 0.38 | 0.45 | 0.0 | 0.0 | 0.0 |
| LOCK_6 cm_J105137+572940 | 0.948 | 0.017 | 1.214 | 0.022 | 10 51 37.01 | 57 29 40.6 | 0.36 | 0.43 | 4.7 | 4.2 | 41.7 |
| LOCK_6 cm_J105143+572938 | 0.074 | 0.014 | 0.238 | 0.046 | 10 51 43.77 | 57 29 38.7 | 0.59 | 0.92 | 9.1 | 6.0 | 8.9 |
| LOCK_6 cm_J105143+573213 | 0.071 | 0.016 | 0.071 | 0.016 | 10 51 43.08 | 57 32 13.5 | 0.57 | 0.64 | 0.0 | 0.0 | 0.0 |
| LOCK_6 cm_J105148+573248A | 2.135 | 0.012 | 3.478 | 0.019 | 10 51 44.16 | 57 33 14.1 | 0.36 | 0.44 | 24.0 | 5.4 | 9.2 |
| LOCK_6 cm_J105148+573248B | 0.531 | 0.015 | 0.635 | 0.018 | 10 51 48.73 | 57 32 48.4 | 0.36 | 0.43 | 4.5 | 4.2 | −31.3 |
| LOCK_6 cm_J105148+573248C | 0.228 | 0.013 | 0.477 | 0.028 | 10 51 56.32 | 57 32 3.2 | 0.40 | 0.45 | 7.1 | 4.4 | −54.1 |
| LOCK_6 cm_J105148+573248T | 2.135 | 0.012 | 5.032 | 0.027 | 10 51 48.73 | 57 32 48.4 | – | – | – | – | – |
| LOCK_6 cm_J105150+572635 | 0.192 | 0.013 | 0.192 | 0.013 | 10 51 50.12 | 57 26 35.5 | 0.38 | 0.45 | 0.0 | 0.0 | 0.0 |
| LOCK_6 cm_J105150+573245 | 0.094 | 0.014 | 0.141 | 0.021 | 10 51 50.32 | 57 32 45.3 | 0.43 | 0.56 | 9.4 | 4.5 | 32.4 |
| LOCK_6 cm_J105156+573322 | 0.067 | 0.014 | 0.067 | 0.014 | 10 51 56.47 | 57 33 22.4 | 0.45 | 0.48 | 0.0 | 0.0 | 0.0 |
| LOCK_6 cm_J105158+572330 | 0.125 | 0.014 | 0.125 | 0.014 | 10 51 58.97 | 57 23 30.4 | 0.41 | 0.47 | 0.0 | 0.0 | 0.0 |
| LOCK_6 cm_J105210+573317 | 0.062 | 0.012 | 0.062 | 0.012 | 10 52 10.14 | 57 33 17.5 | 0.41 | 0.76 | 0.0 | 0.0 | 0.0 |
| LOCK_6 cm_J105211+572907 | 0.485 | 0.011 | 0.485 | 0.011 | 10 52 11.02 | 57 29 8.0 | 0.36 | 0.43 | 0.0 | 0.0 | 0.0 |
| LOCK_6 cm_J105212+572453 | 0.124 | 0.012 | 0.124 | 0.012 | 10 52 12.49 | 57 24 53.0 | 0.39 | 0.45 | 0.0 | 0.0 | 0.0 |
| LOCK_6 cm_J105213+572650 | 0.070 | 0.011 | 0.070 | 0.011 | 10 52 13.33 | 57 26 50.5 | 0.46 | 0.49 | 0.0 | 0.0 | 0.0 |
| LOCK_6 cm_J105216+573529 | 0.076 | 0.013 | 0.076 | 0.013 | 10 52 16.61 | 57 35 30.0 | 0.48 | 0.53 | 0.0 | 0.0 | 0.0 |
| LOCK_6 cm_J105225+573322 | 0.928 | 0.012 | 1.625 | 0.021 | 10 52 25.63 | 57 33 22.5 | 0.36 | 0.43 | 6.1 | 4.5 | 71.4 |
| LOCK_6 cm_J105226+573711 | 0.080 | 0.015 | 0.080 | 0.015 | 10 52 26.79 | 57 37 11.1 | 0.65 | 0.56 | 0.0 | 0.0 | 0.0 |
| LOCK_6 cm_J105227+573832 | 0.091 | 0.020 | 0.091 | 0.020 | 10 52 27.69 | 57 38 32.1 | 0.43 | 0.56 | 0.0 | 0.0 | 0.0 |
| LOCK_6 cm_J105229+573334 | 0.054 | 0.011 | 0.054 | 0.011 | 10 52 29.99 | 57 33 34.6 | 0.47 | 0.54 | 0.0 | 0.0 | 0.0 |
| LOCK_6 cm_J105231+573027 | 0.068 | 0.011 | 0.068 | 0.011 | 10 52 31.13 | 57 30 27.1 | 0.48 | 0.63 | 0.0 | 0.0 | 0.0 |
| LOCK_6 cm_J105231+573204 | 0.067 | 0.011 | 0.067 | 0.011 | 10 52 31.48 | 57 32 5.0 | 0.53 | 0.51 | 0.0 | 0.0 | 0.0 |
| LOCK_6 cm_J105231+573501 | 0.076 | 0.012 | 0.076 | 0.012 | 10 52 31.08 | 57 35 1.4 | 0.63 | 0.48 | 0.0 | 0.0 | 0.0 |
| LOCK_6 cm_J105233+573057 | 0.231 | 0.011 | 0.231 | 0.011 | 10 52 33.99 | 57 30 57.1 | 0.37 | 0.44 | 0.0 | 0.0 | 0.0 |
| LOCK_6 cm_J105234+572643 | 0.054 | 0.011 | 0.054 | 0.011 | 10 52 34.84 | 57 26 43.6 | 0.43 | 0.54 | 0.0 | 0.0 | 0.0 |
| LOCK_6 cm_J105235+572640 | 0.054 | 0.011 | 0.054 | 0.011 | 10 52 35.19 | 57 26 40.2 | 0.77 | 0.59 | 0.0 | 0.0 | 0.0 |
| LOCK_6 cm_J105237+572147 | 0.059 | 0.013 | 0.059 | 0.013 | 10 52 37.34 | 57 21 47.1 | 0.60 | 0.52 | 0.0 | 0.0 | 0.0 |
| LOCK_6 cm_J105237+573104A | 4.376 | 0.012 | 5.823 | 0.015 | 10 52 36.40 | 57 30 46.9 | 0.36 | 0.43 | 4.6 | 4.4 | −41.8 |
| LOCK_6 cm_J105237+573104B | 0.750 | 0.012 | 2.863 | 0.045 | 10 52 37.39 | 57 31 04.1 | 0.36 | 0.43 | 6.9 | 5.7 | 21.2 |
| LOCK_6 cm_J105237+573104C | 1.101 | 0.011 | 3.384 | 0.034 | 10 52 37.77 | 57 31 12.3 | 0.36 | 0.43 | 10.0 | 5.8 | 12.3 |
| LOCK_6 cm_J105237+573104D | 2.172 | 0.012 | 3.770 | 0.020 | 10 52 38.17 | 57 31 20.3 | 0.36 | 0.43 | 4.9 | 4.2 | −89.1 |
| LOCK_6 cm_J105237+573104T | 4.376 | 0.012 | 16.452 | 0.044 | 10 52 37.05 | 57 30 58.8 | – | – | – | – | – |
| LOCK_6 cm_J105238+572221 | 0.057 | 0.012 | 0.057 | 0.012 | 10 52 38.78 | 57 22 21.4 | 0.57 | 0.59 | 0.0 | 0.0 | 0.0 |
| LOCK_6 cm_J105238+573321 | 0.053 | 0.011 | 0.053 | 0.011 | 10 52 38.00 | 57 33 21.4 | 0.50 | 0.51 | 0.0 | 0.0 | 0.0 |
| LOCK_6 cm_J105239+572430 | 0.058 | 0.011 | 0.058 | 0.011 | 10 52 39.54 | 57 24 30.7 | 0.61 | 0.53 | 0.0 | 0.0 | 0.0 |
| LOCK_6 cm_J105241+572320 | 0.812 | 0.011 | 0.812 | 0.011 | 10 52 41.45 | 57 23 20.6 | 0.36 | 0.43 | 0.0 | 0.0 | 0.0 |
| LOCK_6 cm_J105242+571915 | 0.101 | 0.017 | 0.160 | 0.027 | 10 52 42.47 | 57 19 15.8 | 0.66 | 0.81 | 8.5 | 4.3 | 38.4 |
| LOCK_6 cm_J105245+573615 | 0.239 | 0.013 | 0.239 | 0.013 | 10 52 45.35 | 57 36 15.9 | 0.38 | 0.44 | 0.0 | 0.0 | 0.0 |
| LOCK_6 cm_J105249+573626 | 0.070 | 0.013 | 0.070 | 0.013 | 10 52 49.73 | 57 36 26.6 | 0.66 | 0.59 | 0.0 | 0.0 | 0.0 |
| LOCK_6 cm_J105252+572859 | 0.062 | 0.011 | 0.098 | 0.018 | 10 52 52.79 | 57 28 59.7 | 0.71 | 0.50 | 6.5 | 4.8 | 84.6 |
| LOCK_6 cm_J105254+572341 | 0.131 | 0.011 | 0.131 | 0.011 | 10 52 54.27 | 57 23 41.7 | 0.39 | 0.45 | 0.0 | 0.0 | 0.0 |
| LOCK_6 cm_J105255+571950 | 1.015 | 0.017 | 1.015 | 0.017 | 10 52 55.32 | 57 19 50.6 | 0.36 | 0.43 | 0.0 | 0.0 | 0.0 |
| LOCK_6 cm_J105259+573226 | 0.164 | 0.011 | 0.164 | 0.011 | 10 52 59.34 | 57 32 26.1 | 0.38 | 0.46 | 0.0 | 0.0 | 0.0 |
| LOCK_6 cm_J105301+572521 | 0.103 | 0.011 | 0.103 | 0.011 | 10 53 1.69 | 57 25 21.2 | 0.40 | 0.47 | 0.0 | 0.0 | 0.0 |
| LOCK_6 cm_J105301+573333 | 0.052 | 0.011 | 0.052 | 0.011 | 10 53 1.48 | 57 33 34.0 | 1.01 | 0.51 | 0.0 | 0.0 | 0.0 |
| LOCK_6 cm_J105303+573429 | 0.067 | 0.012 | 0.067 | 0.012 | 10 53 3.38 | 57 34 29.1 | 0.50 | 0.51 | 0.0 | 0.0 | 0.0 |
| LOCK_6 cm_J105303+573526 | 0.072 | 0.013 | 0.072 | 0.013 | 10 53 3.28 | 57 35 26.9 | 0.50 | 0.53 | 0.0 | 0.0 | 0.0 |
| LOCK_6 cm_J105303+573532 | 0.079 | 0.014 | 0.143 | 0.025 | 10 53 3.91 | 57 35 32.2 | 0.48 | 0.70 | 6.6 | 4.6 | −7.7 |
| LOCK_6 cm_J105304+573055 | 0.183 | 0.011 | 0.183 | 0.011 | 10 53 4.83 | 57 30 55.9 | 0.37 | 0.45 | 0.0 | 0.0 | 0.0 |
| LOCK_6 cm_J105308+572223 | 0.191 | 0.013 | 0.191 | 0.013 | 10 53 8.09 | 57 22 23.0 | 0.38 | 0.45 | 0.0 | 0.0 | 0.0 |

**Table 1.** continued.

| Name | $S_P$ (mJy) | $\sigma_{S_P}$ (mJy) | $S_T$ (mJy) | $\sigma_{S_T}$ (mJy) | RA (J2000) | Dec (J2000) | $\sigma_\alpha$ ($''$) | $\sigma_\delta$ ($''$) | $\theta_M$ ($''$) | $\theta_m$ ($''$) | PA deg |
|---|---|---|---|---|---|---|---|---|---|---|---|
| LOCK_6 cm_J105308+573436 | 0.083 | 0.012 | 0.083 | 0.012 | 10 53 8.65 | 57 34 36.7 | 0.44 | 0.46 | 0.0 | 0.0 | 0.0 |
| LOCK_6 cm_J105310+573434 | 0.064 | 0.012 | 0.064 | 0.012 | 10 53 10.57 | 57 34 34.8 | 0.47 | 0.53 | 0.0 | 0.0 | 0.0 |
| LOCK_6 cm_J105312+573111 | 0.097 | 0.011 | 0.097 | 0.011 | 10 53 12.70 | 57 31 11.9 | 0.42 | 0.52 | 0.0 | 0.0 | 0.0 |
| LOCK_6 cm_J105313+572507 | 0.079 | 0.011 | 0.079 | 0.011 | 10 53 13.89 | 57 25 7.4 | 0.53 | 0.46 | 0.0 | 0.0 | 0.0 |
| LOCK_6 cm_J105314+572448 | 0.091 | 0.012 | 0.147 | 0.020 | 10 53 14.01 | 57 24 48.8 | 0.47 | 0.52 | 5.4 | 4.7 | 49.9 |
| LOCK_6 cm_J105314+573020 | 0.093 | 0.012 | 0.143 | 0.018 | 10 53 14.20 | 57 30 20.6 | 0.51 | 0.48 | 6.1 | 4.0 | −67.4 |
| LOCK_6 cm_J105316+573551 | 0.088 | 0.015 | 0.088 | 0.015 | 10 53 16.74 | 57 35 51.7 | 0.54 | 0.58 | 0.0 | 0.0 | 0.0 |
| LOCK_6 cm_J105317+572722 | 0.053 | 0.011 | 0.053 | 0.011 | 10 53 17.39 | 57 27 22.4 | 0.65 | 0.51 | 0.0 | 0.0 | 0.0 |
| LOCK_6 cm_J105322+573652 | 0.100 | 0.019 | 0.100 | 0.019 | 10 53 22.37 | 57 36 52.9 | 0.49 | 0.56 | 0.0 | 0.0 | 0.0 |
| LOCK_6 cm_J105325+572911 | 0.200 | 0.012 | 0.200 | 0.012 | 10 53 25.30 | 57 29 11.5 | 0.38 | 0.44 | 0.0 | 0.0 | 0.0 |
| LOCK_6 cm_J105327+573316 | 0.128 | 0.013 | 0.128 | 0.013 | 10 53 27.46 | 57 33 16.6 | 0.39 | 0.50 | 0.0 | 0.0 | 0.0 |
| LOCK_6 cm_J105328+573535 | 0.084 | 0.017 | 0.084 | 0.017 | 10 53 28.92 | 57 35 35.8 | 0.56 | 0.52 | 0.0 | 0.0 | 0.0 |
| LOCK_6 cm_J105335+572157 | 0.093 | 0.021 | 0.144 | 0.032 | 10 53 35.78 | 57 21 57.3 | 0.59 | 0.80 | 6.7 | 4.7 | −31.4 |
| LOCK_6 cm_J105335+572921 | 0.109 | 0.013 | 0.109 | 0.013 | 10 53 35.18 | 57 29 21.3 | 0.41 | 0.49 | 0.0 | 0.0 | 0.0 |
| LOCK_6 cm_J105342+573026 | 0.124 | 0.014 | 0.124 | 0.014 | 10 53 42.08 | 57 30 26.5 | 0.43 | 0.46 | 0.0 | 0.0 | 0.0 |
| LOCK_6 cm_J105347+573349 | 0.172 | 0.020 | 0.172 | 0.020 | 10 53 47.14 | 57 33 49.5 | 0.41 | 0.47 | 0.0 | 0.0 | 0.0 |
| LOCK_6 cm_J105348+573033 | 0.088 | 0.016 | 0.088 | 0.016 | 10 53 48.73 | 57 30 33.8 | 0.46 | 0.52 | 0.0 | 0.0 | 0.0 |

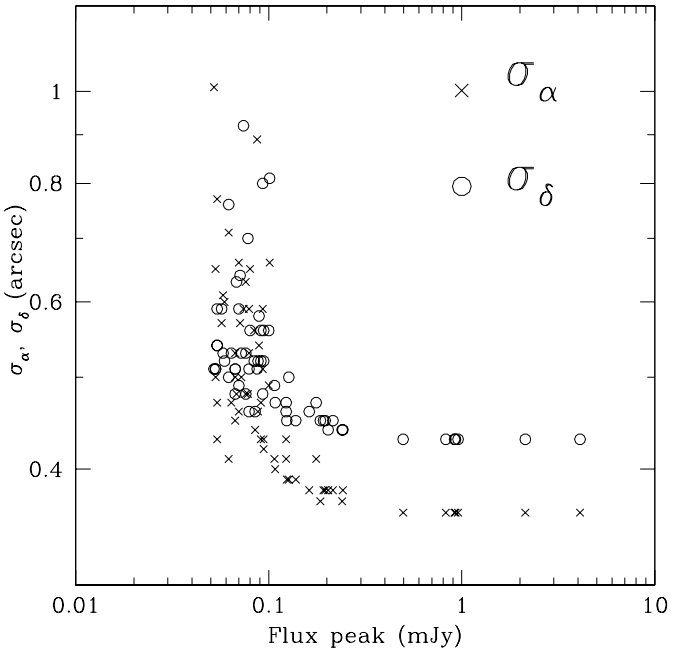


**Fig. 6.** The position uncertainties $\sigma_\alpha$ and $\sigma_\delta$ for all the sources in the 6 cm catalogue as a function of the peak flux density $S_P$.

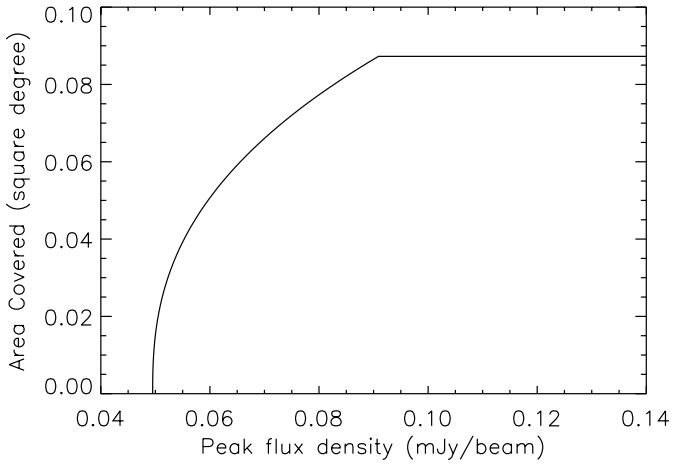


**Fig. 7.** Areal coverage of the Lockman Hole at 6 cm represented by the solid angle over which a source with peak flux $S_P$ can be detected.

comparison between the total number of sources detected in each bin (from the five simulations) and the total number of sources in the input sample in the same bin we calculated the correction factor $C$ to be applied to our observed source counts due to the incompleteness of the survey.

### 3.3.2. Source counts

For comparison with other 6 cm studies, the source counts are normalized to a non evolving Euclidean model which fits the brightest sources in the sky. At 6 cm the standard Euclidean integral counts are $N(>S_{6\ \mathrm{cm}}) = 60 \times S_{6\ \mathrm{cm}}^{-1.5}$ sr$^{-1}$, with $S_{6\ \mathrm{cm}}$ expressed in Jy. The results are given in Table 2 where, for each bin, we report the flux interval, the average flux, the number of sources detected ($N$), the correction factor $C$, the number of sources after that the correction factor has been applied ($N_c$), the expected number of sources for a static Euclidean universe ($N_{exp}$) and the normalized counts $N_c/N_{exp}$. The estimated error is $N_c^{1/2}/N_{exp}$. The average flux in each bin has been assumed equal to the geometric mean of the bin flux limits. Since in the flux interval sampled in our survey (∼0.1–1.0 mJy) the best fit slope $\gamma$ of the normalized differential counts (d$N$/d$S$ $\propto S^{-\gamma}$) is $\gamma \sim 2.0$ (Donnelly et al. 1987), this assumption is formally correct. In fact, only when $\gamma = 2.0$ the value of the average flux is equal to the geometric mean (Windhorst et al. 1984).

Our results are compared with previous work in Fig. 8. In this figure we show only the source counts below ∼100 mJy. Above this flux the source counts are well known, with an

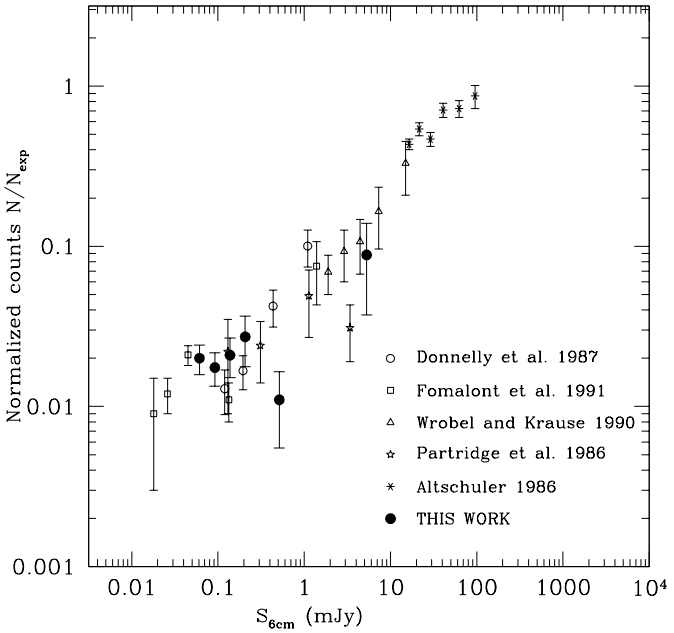


**Fig. 8.** Differential 6 cm source counts normalized to a Euclidean Universe. Filled circles are our 6 cm counts in the Lockman Hole. The open points come from Donnelly et al. (1987), Fomalont et al. (1991), Wroble & Krause (1990) and Partridge et al. (1986). The six points above 15 mJy come from Altschuler (1986).

initial steep rise between $S \simeq 10$ and $S \simeq 1$ Jy, a maximum excess with respect the Euclidean prediction between $S \simeq 1.0$ Jy and $S \simeq 0.1$ Jy and a subsequent continuous convergence between $S \simeq 100$ and $S \simeq 3$ mJy. Below $S \simeq 3$ mJy there is a clear flattening in the slope of the 6cm radio source counts (see Windhorst et al. (1993) for a review of the radio source counts at different frequencies down to the microjansky level).

As illustrated in figure, there is a reasonably good agreement between the Lockman 6 cm counts and those obtained by other surveys in the same flux range, confirming that there is no strong indication for a significant change in slope in the 6 cm counts between ~0.1 and 1 mJy. Although the statistics is relatively poor, a possible flattening in the differential counts is instead suggested at fluxes below ~0.1 mJy.

## 4. Radio, optical and X-ray associations

### 4.1. Coincidences with 20 centimeter sources

Forty-four of the 149 sources in the $4\sigma$ radio sample at 20 cm published in de Ruiter et al. (1997) are within the 6 cm map. Two of these sources have more than one component (sources 71 and 99, see Table 1 in de Ruiter et al. 1997). When a compact 20 cm radio source is within 5″ from the 6 cm position, we accepted it as a real coincidence. Thus a 6 cm source was considered to be the counterpart of a 20 cm source only if the difference in position was significantly less than the one beam radius (the 20 cm map has been restored with a beam of ~12″, see de Ruiter et al. 1997). However, for extended 20 cm radio sources, we allowed a maximum distance of 10″ between the 20 cm and 6 cm positions. This is a necessary requirement in order not to miss 20–6 cm coincidences of low surface brightness sources. We find a total of 32 coincidences. Except for a few extended sources, the 20−6 cm positional correspondence is usually better than 3 arcsec. No other pair of 6–20 cm sources has been found at distances in the range 5–10 arcsec.

Since the 6 and 20 cm surveys have two different beams ($4 \times 4$ arcsec and $12 \times 12$ arcsec respectively), the spectral indices $\alpha$ ($S \propto \nu^{-\alpha}$) for all the coincidences were calculated using the total 20 cm fluxes reported in de Ruiter et al. (1997) and the integrated 6 cm fluxes obtained after convolving the 6 cm map with the same beam width as the 20 cm image. For 42 of the 63 radio sources the differences between the 6 cm fluxes obtained from the maps with the two different beam sizes are smaller than 20%, while only 4 sources show a difference between the two fluxes greater than a factor 1.7 (up to a factor 2.1). However these 4 sources have all a radio flux density lower than 0.1 mJy and have not been considered in the statistical analysis of the radio spectral index (see Sect. 5.1). The error in each calculated value of spectral index was computed by taking the quadrature sum of the relative errors in the two flux densities $S_1$ and $S_2$:

$$\sigma_\alpha = \sqrt{(\sigma_{S_1}/S_1)^2 + (\sigma_{S_2}/S_2)^2}/(\ln \nu_2 - \ln \nu_1) \quad (3)$$

with $\nu_1 = 1490$ MHz and $\nu_2 = 4860$ MHz. For the 6 cm sources without a 20 cm counterpart, we calculated a $4\sigma$20 cm upper limit using $\sigma(\mu Jy) = 0.14r^2 - 1.78r + 34.4$, where $r$ is the distance (in arcmin) from the 20 cm image center (de Ruiter et al. 1997).

The results of the 20–6 cm cross-correlation are summarized in Table 3, where, for each 6 cm source we report the optical identification (Cols. 2–9, see below), the name of the 20 cm counterpart (from Table 1 of de Ruiter et al. 1997), the 20 cm flux density (or $4\sigma$ upper limit), the radio spectral index (or upper limit) and the distance between the two radio positions.

The two 20 cm sources with more than one component (71 and 99) have been associated with multi component 6 cm sources. In particular the triple source 71 has been associated with the three component LOCK_6 cm J105148+573248. For this source we found a good agreement between the position of the components detected at the two radio frequencies. More complex is the situation for the other source (99). This double source at 20 cm has been resolved into a four component source (LOCK_6 cm J105237+573104) in the 6 cm map.

Moreover, a new, relatively bright radio source (LOCK_6 cm_J105233+573057, $S_{\rm total} = 0.241$ mJy) has been detected at a distance of 25″ from the geometric center of the multiple source. This new radio source has a very unusual inverted radio spectral index ($\alpha_{\rm r} < -0.48$) and an optical counterpart that shows a clear extension in the direction of the multiple radio source. A 6 cm contour plot superimposed on the $V$ band CCD image is shown in Fig. 9.

For the two multiple sources we report in Table 3 only the spectral index derived from the total integrated flux.

**Table 2.** Counts of radio sources.

| Flux Density Range (mJy) | | Average (mJy) | Number Sources ($N$) | $C$ | Corrected Number Sources ($N_c$) | $N_{exp}$ | $N_c/N_{exp}$ ($\times 10^{-2}$) |
|---|---|---|---|---|---|---|---|
| 0.050 | 0.075 | 0.061 | 18 | 1.26 | 22.7 | 1135 | $2.00 \pm 0.42$ |
| 0.075 | 0.113 | 0.092 | 17 | 1.10 | 18.7 | 1064 | $1.75 \pm 0.41$ |
| 0.113 | 0.169 | 0.138 | 12 | 1.05 | 12.6 | 602 | $2.09 \pm 0.58$ |
| 0.169 | 0.253 | 0.207 | 9 | 1.00 | 9.0 | 330 | $2.72 \pm 0.91$ |
| 0.253 | 1.281 | 0.569 | 4 | 1.00 | 4.0 | 362 | $1.10 \pm 0.55$ |
| 1.281 | 21.895 | 5.296 | 3 | 1.00 | 3.0 | 34 | $8.82 \pm 5.09$ |

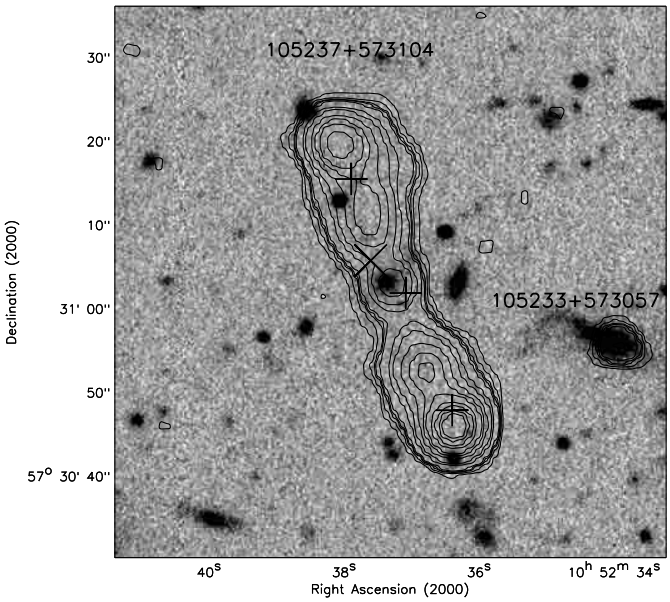


**Fig. 9.** 6 cm radio contour plot of the sources LOCK_6 cm J105237+573104 and LOCK_6 cm J105233+573057 superimposed on the $V$ band CCD image. The three + symbols represent the position of the 20 cm source 99 (99a, 99* and 99b for increasing RA), while the symbol X represents the position of the X-ray source 116 identified by Lehmann et al. (2000) with the galaxy near the radio centroid.

### 4.2. Optical identification of 6 cm radio sources

The entire 6 cm field is covered by $V$ and $I$ CCD data collected at the Canada-France-Hawaii Telescope (CFHT) with the UH8K camera (see Wilson et al. 2001 and Kaiser et al. 2001 for a description of these data). The approximate limits in the two bands are $V \sim 25.5$ mag and $I \sim 24.5$ mag for point sources (Vega – magnitude). The CCD field is $30' \times 30'$ around the ROSAT ultra deep *HRI* and 6 cm field center. Moreover, a mosaic of $K'$-band images (from the Omega-Prime camera on the Calar Alto 3.5-m telescope) covering the field in a non-uniform fashion with gaps in between is also available (see Lehmann et al. 2000 and Schmidt et al. 1998 for a summary of the optical available data in the Lockman Hole). The limiting magnitudes of the $K'$ images is $K' \sim 20.2$ mag. The typical photometric error on the $V$, $I$ and $K'$ magnitudes is ~0.1 mag.

#### 4.2.1. Identification in the $V$ and $I$ bands

For the optical identification of the 6 cm radio sources, we used the likelihood ratio technique described by Sutherland & Saunders (1992). The mean off-set between the radio and optical positions estimated in Sect. 3.2 has been subtracted from the radio positions to compute the positional offset $r$. For a given optical candidate with magnitude $m$ and positional offset $r$ from the radio source position, we calculate the probability $p$ that the true source lies in an infinitesimal box $r \pm dr/2$, and in a magnitude interval $m \pm dm/2$; on the assumption that the positional offsets are independent of the *optical* properties $p$ is given by:

$$p = q(m)\, dm \times 2\pi\, r\, f(r)\, dr, \tag{4}$$

where $f(r)$ is the probability distribution function of the positional errors, assumed to be equal in the two coordinates, with

$$2\pi \int_0^{+\infty} f(r)\, r\, dr = 1 \tag{5}$$

and $q(m)$ is the expected distribution as a function of magnitude of the optical counterparts.

The likelihood ratio $LR$ is defined as the ratio between the probability that the source is the correct identification and the corresponding probability for a background, unrelated object:

$$LR = \frac{q(m) f(r)}{n(m)} \tag{6}$$

where $n(m)$ is the surface density of background objects with magnitude $m$.

The presence or absence of other optical candidates for the same radio source provides *additional information* to that contained in $LR$. Thus a self-consistent formula has been developed for the reliability of each individual object, taking this information into account (Sutherland & Saunders 1992). The reliability $\mathrm{Rel}_j$ for object $j$ being the correct identification is:

$$\mathrm{Rel}_j = \frac{(LR)_j}{\Sigma_i (LR)_i + (1 - Q)} \tag{7}$$

where the sum is over the set of all candidates for this particular source and $Q$ is the probability that the optical counterpart of the source is brighter than the magnitude limit of the optical catalogue ($Q = \int^{m_{\mathrm{lim}}} q(m)\, dm$).

In order to derive an estimate for $q(m)$ we have first counted all objects in the optical catalogue within a fixed radius around

each source (total*(m)*). This distribution has then been background subtracted

$$\text{real}(m) = [\text{total}(m) - n(m) * N_{\text{radio sources}} * \pi * \text{radius}^2] \quad (8)$$

and normalized to construct the distribution function of "real" identifications:

$$q(m) = \frac{\text{real}(m)}{\Sigma_i \text{real}(m)_i} \times Q \quad (9)$$

where $\Sigma_i$ is the sum over all the magnitude bins of the distribution, i.e. is the total number of objects in the real($m$) distribution.

In order to maximize the statistical significance of the over density due to the presence of the optical counterparts, we have adopted for the radius the minimum size which assures that most of the possible counterparts are included within such radius. On the basis of the positional uncertainties shown in Fig. 6, we have adopted a radius of 2 arcsec. Figure 10 shows the resulting real*(m)* distribution (dotted line) together with the expected distribution of background objects (solid line), i.e. objects unrelated to the radio sources. The smooth curve fitted to the real($m$) distribution (dot dot dot dashed line) has been normalized according to Eq. (9) and then used as input in the likelihood calculation. The total number of objects in the real($m$) distribution is 48.8 ± 8.7. Since the number of radio sources is 63, this corresponds to an expected fraction of identifications above the magnitude limit of the optical catalogue of the order of (77 ± 14)%. On this basis we adopted $Q = 0.8$. This value is also in agreement with the results obtained by Hammer et al. (1995) for the radio sources in the Canada-France Redshift Survey and by Fomalont et al. (1997) and Richards et al. (1998) for the radio sources in the Hubble Deep Field (HDF). Using $I$ band CCD data with a magnitude limit of $I \sim 24.5$ mag Hammer et al. found 32 optical identifications for 36 radio sources with $S_{5.0\ \text{GHz}} > 16\ \mu$Jy, while Richards et al. found 26 optical counterparts down to $I = 25$ mag for 29 radio sources with $S_{8.5\ \text{GHz}} > 9\ \mu$Jy.

However, to check how this assumption could affect our results, we repeated the likelihood ratio analysis using different values of $Q$ in the range 0.5–1.0. No substantial difference in the final number of identifications and in the associated reliability (see below) has been found.

As probability distribution of positional errors we adopted a Gaussian distribution with standard deviation, $\sigma$, which takes into account the combined effect of the radio and the optical positional uncertainties:

$$f(r) = \frac{1}{2\pi\sigma^2} \exp\left(\frac{-r^2}{2\sigma^2}\right). \quad (10)$$

For each source the value of $\sigma$ used is the average value between $\sigma_x = \sqrt{\text{er}_{\text{op}}^2 + \sigma_\alpha^2}$ and $\sigma_y = \sqrt{\text{er}_{\text{op}}^2 + \sigma_\delta^2}$, where $\text{er}_{\text{op}}$ is the error on the optical position (we assumed a value of 0.5 arcsec), while $\sigma_\alpha$ and $\sigma_\delta$ are the radio positional errors in RA and Dec reported in Table 1.

Having determined the values of *q(m)*, *f(r)* and *n(m)*, we computed the *LR* value for all the optical sources within a distance of 5 arcsec from the radio position. Once that the *LR* values have been computed for all the optical candidates, one has

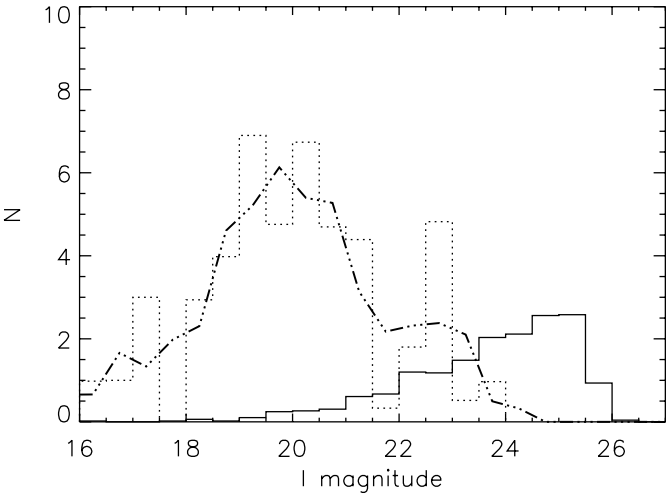


**Fig. 10.** Magnitude distributions of background objects (solid line) and 'real' detections (real*(m)*, dotted line) estimated from the optical objects detected in the $I$ band within a radius of 2 arcsec around each radio sources. The smooth curve fitted to the real*(m)* distribution (dot dot dot dashed line) has been normalized according to Eq. (9) and then used as input in the likelihood calculation.

to choose the best threshold value for $LR$ ($L_{\text{th}}$) to discriminate between spurious and real identifications. The choice of $L_{\text{th}}$ depends on two factors: first, it should be small enough to avoid missing many real identifications and having a rather incomplete sample. Secondly, $L_{\text{th}}$ should be large enough to keep the number of spurious identifications as low as possible and to increase the reliability.

As $LR$ threshold we adopted $L_{\text{th}} = 0.2$. With this value, according to Eq. (7) and considering that our estimate for $Q$ is 0.8, all the optical counterparts of radio sources with only one identification (the majority in our sample) and $LR > LR_{\text{th}}$ have a reliability greater than 0.5. This choice also approximately maximizes the sum of sample reliability and completeness.

With this threshold value we find 56 radio sources with a likely identification (three of which have two optical candidates with $L_{\text{th}} > 0.20$ for a total of 59 optical candidates with $L_{\text{th}} > 0.20$).

The reliability (Rel) of each of these optical identifications (see Eq. (7)) is always high (>95 per cent for most of the sources), except for the few cases where more than one optical candidate with $L_{\text{th}} > 0.20$ is present for the same radio source.

The number of expected real identifications (obtained adding the reliability of all the objects with $L_{\text{th}} > 0.20$) is about 53 i.e. we expect that about 3 of the 56 proposed radio-optical associations may be spurious positional coincidences. Similar results are obtained using the catalogue in the $V$ band. The results of the optical identification are summarized in Table 3. For each radio source we report all the optical counterparts within 3 arcsec and with a magnitude $I \leq 24.5$ plus two objects which, having $I > 24.5$ mag, are too faint for a reliable determination of their likelihood ratio, but we however considered as likely identification because of their small distance (lower than 0.6 arcsec)

from the radio position (LOCK_6 cm_J105158+573330 and LOCK_6 cm_105259+573226).

In the three cases in which more than one optical object with $LR > LR_{\rm th}$ have been found associated to the same radio source, we assumed the object with the highest Likelihood Ratio value as the counterpart of this radio source.

#### 4.2.2. Identification in the $K'$ band

As said above, the $K'$ band data cover the 6 cm field in a non-uniform fashion. For 12 of the 63 radio sources $K'$ band data are not available. Since all the 51 radio sources with available $K'$ band data do have an optical identification in the $I$ band, we looked for $K'$ counterparts using a maximum distance of 1.0 arcsec from the optical position. We found a $K'$ counterpart for 49 of the 51 radio sources. The same results is obtained using a search radius of 2 arcsec.

A summary of the results of our identifications is given in Table 3. For each radio source, we give the $V$, $I$ and $K'$ magnitude (when available), the total distance and the distance in RA and Dec between the radio and the optical position and the Likelihood Ratio and reliability values obtained using the $I$ band catalogue. For the radio sources with more than one optical counterpart we assumed as the real identification the optical source with the highest reliability. A blank field in the $K'$ magnitude column means no data available.

In summary, considering as good identifications also the two sources fainter than $I \sim 24.5$ mag, we have a proposed identification for 58 of the 63 radio sources (92 per cent): ~54 of these are likely to be the correct identification. Moreover, for a subsample of 51 radio sources (all of them with an optical identification in $I$) we have information also in the $K'$ band. For this subsample we found $K'$ counterparts for 49 sources (96 per cent of identifications).

### 4.3. X-ray counterparts

The area from which we have extracted our radio catalogue (10 arcmin radius) has been covered by the ROSAT Ultra Deep Survey (about 1 million seconds of exposure with the *HRI*) reaching a limiting flux of about $1.2 \times 10^{-15}$ erg cm$^{-2}$ s$^{-1}$ in the 0.5–2.0 keV energy band. The *HRI* catalogue (Lehmann et al. 2001) lists 54 sources in this area. A cross- correlation was performed between the position of the 54 X-ray sources and the 63 radio sources detected at 6 cm. We find 8 reliable radio/X-ray associations with a positional difference smaller than 5 arcsec. An additional radio/X-ray association is found with the PSPC source 116 (Hasinger et al. 1998) which was not detected with the *HRI*. At these fluxes ($S_{0.5-2.0\ \rm keV} \sim 1.2 \times 10^{-15}$ erg cm$^{-2}$ s$^{-1}$, $S_{6\ \rm cm} \sim 50\ \mu$Jy) the surface densities of radio and X-ray sources are similar and the coincidences between the samples selected at radio and X-ray frequencies are about 15%. All these nine radio/X-ray sources have been optically identified by Lehmann et al. (2000) and Lehmann et al. (2001). The radio/X-ray associations are given in Table 4. For each radio source we report the radio flux, the radio spectral index $\alpha_{\rm r}$, the $I$ and $K'$ band magnitude, the name of the X-ray counterpart, the distance between the radio and X-ray position, the ROSAT *HRI* (except for source 116 for which we have the ROSAT-PSPC flux) 0.5–2.0 keV flux of the X-ray source in units of $10^{-14}$ erg cm$^{-2}$ s$^{-1}$, the optical classification (1 for type I AGN, 2 for type II AGN and 3 for cluster), the redshift and the radio luminosity in W/Hz ($H_0 = 70$ km s$^{-1}$ Mpc$^{-1}$, $\Omega_{\rm M} = 0.3$, $\Omega_\lambda = 0.7$).

Recently the Lockman Hole has been observed also with the XMM-Newton satellite (Hasinger et al. 2001; Lehmann et al. 2002). The center of the XMM-Newton observation is coincident with the ROSAT *HRI* field center and with the 6 cm survey discussed in this paper. A total of ~100 ksec good exposure time has been accumulated, reaching a flux limit of $3.8 \times 10^{-16}$ erg cm$^{-2}$ s$^{-1}$ in the 0.5–2.0 keV band. Within an off-axis angle of 10 arcmin (i.e. the same region of the sky that we used to extract the 6 cm radio sources) a total of 106 sources have been detected (see Lehmann et al. 2002). In addition to the 9 radio/X-ray associations already found with the ROSAT data, there are four new radio/X-ray associations with the XMM-Newton source list. The percentage of XMM/X-ray sources with a radio counterpart is therefore ~12.3 per cent (13/106). The properties of the new radio/XMM associations are reported in the last 4 lines of Table 4.

It is interesting to note that out of 13 radio/X-ray associations, eight (62%) are classified as type II AGN. Eight of the 13 radio sources are detected at both 21 and 6 cm and all of them have steep spectral indices ($\alpha_{\rm r} > 0.4$). For the five sources not detected at 21 cm the upper limits in $\alpha_{\rm r}$ show that two have a flat, inverted spectrum ($\alpha_{\rm r} < -0.06$ and $\alpha_{\rm r} < 0.21$), while the other three can have both steep and flat spectra. The two multiple radio sources (LOCK_6 cm J105148+573248T and LOCK_6 cm J105237+573104T) and the sources LOCK_6 cm J105255+571950 and LOCK_6 cm J105347+573349 can be classified as type II Fanaroff-Riley (FRII) radio galaxies on the basis of their morphology and their radio luminosity (greater than $10^{24.9}$ W/Hz, see last column of Table 4), while all the other 9 radio/X-ray associations have radio luminosities typical of FRI radio galaxies ($L_{5\ \rm GHz} < 10^{24.0}$ W/Hz).

## 5. Discussion

### 5.1. Radio spectral index

The spectral indices $\alpha_{\rm r}$ determined between 20 and 6 cm are listed in Table 3. Our calculation assumes that the radio sources have not varied significantly in the 8 years interval between the 20 cm observations (December 1990) and the 6 cm observations (January 1999) reported here. As shown by Oort & Windhorst (1985) and by Windhorst et al. (1985), a significant variability occurs in only about 5% of the mJy and sub-mJy radio sources population. Hence, the statistical analysis of the spectral index presented below should not be seriously biased by source variability. In our analysis we included both the measured values and the upper limits to $\alpha_{\rm r}$ given in Table 3 and used the software package ASURV which implements the methods described by Feigelson & Nelson (1985) and Isobe et al. (1986).

**Table 3.** Optical, near infrared and 20 cm counterparts of the 6 cm sources in the Lockman Hole.

| NAME | $V^a$ | $I^a$ | $K'^a$ | Δ (″) | ΔRA (″) | ΔDec (″) | $LR$ | Rel. | 20 cm Nr. | $F20$ mJy | $F20_{\rm err}$ | $\alpha_{\rm r}$ | $\alpha_{\rm r\ err}$ | Δ6−20 (″) |
|---|---|---|---|---|---|---|---|---|---|---|---|---|---|---|
| LOCK_6 cm_J105135+572739 | 22.8 | 21.1 | 18.2 | 1.02 | −0.97 | 0.30 | 8.66 | 0.98 | 59 | 0.190 | 0.030 | 0.63 | 0.21 | 2.6 |
| LOCK_6 cm_J105136+572959 | 0.0[b] | 20.4 | 17.8 | 0.81 | −0.81 | 0.09 | 23.83 | 0.98 | 61 | 0.399 | 0.050 | 1.24 | 0.19 | 3.9 |
| LOCK_6 cm_J105136+573302 | 0.0[b] | 21.5 | 18.8 | 1.15 | −0.67 | 0.94 | 2.69 | 0.93 | 60 | 0.447 | 0.040 | 1.01 | 0.15 | 0.5 |
| | 0.0[b] | 21.5 | >20.2 | 2.70 | 0.27 | 2.69 | 0.01 | 0.00 | 60 | 0.447 | 0.040 | 1.01 | 0.15 | 0.5 |
| LOCK_6 cm_J105137+572940 | 0.0[b] | 20.7 | 17.4 | 1.42 | −1.41 | 0.13 | 5.72 | 0.97 | 63 | 2.210 | 0.080 | 0.49 | 0.03 | 0.4 |
| LOCK_6 cm_J105143+572938 | 0.0[b] | 15.4 | 13.5 | 1.62 | −0.60 | 2.55 | 24.66 | 0.99 | 69 | 0.421 | 0.040 | 0.52 | 0.19 | 3.3 |
| LOCK_6 cm_J105143+573213 | 0.0[b] | >24.5 | | | | | - | - | | <0.126 | | <0.65 | | |
| LOCK_6 cm_J105148+573248T | 0.0[b] | 21.4 | 18.0 | 0.72 | −0.40 | 0.59 | 7.71 | 0.97 | 71* | 15.390 | 0.580 | 0.95 | 0.03 | 0.2 |
| LOCK_6 cm_J105150+573245 | 0.0[b] | 18.0 | | 1.41 | −0.50 | 1.31 | 1.87 | 0.90 | | <0.126 | | <−0.06 | | |
| LOCK_6 cm_J105150+572635 | 25.4 | 22.8 | 19.3 | 1.03 | −0.87 | −0.55 | 33.79 | 0.99 | 72 | 0.216 | 0.060 | 0.00 | 0.26 | 2.0 |
| LOCK_6 cm_J105156+573322 | 22.1 | 20.7 | >20.2 | 1.54 | 0.37 | −1.50 | 4.67 | 0.96 | | <0.131 | | <0.70 | | |
| LOCK_6 cm_J105158+572330 | >25.5 | 25.3 | | 0.59 | −0.57 | 0.14 | 0.00 | 0.00 | 74 | 0.195 | 0.030 | 0.47 | 0.17 | 0.6 |
| LOCK_6 cm_J105210+573317 | 23.9 | 22.7 | 19.4 | 1.82 | −0.13 | −1.81 | 0.41 | 0.50 | | <0.131 | | <0.69 | | |
| | 23.5 | 22.3 | 19.6 | 2.02 | −1.34 | 1.52 | 0.22 | 0.26 | | <0.131 | | <0.69 | | |
| LOCK_6 cm_J105211+572907 | 25.5 | 23.6 | 19.3 | 0.67 | −0.64 | −0.20 | 0.77 | 0.79 | 81 | 1.455 | 0.060 | 0.97 | 0.04 | 0.3 |
| LOCK_6 cm_J105212+572453 | 21.6 | 19.8 | 17.1 | 0.52 | −0.50 | −0.14 | 70.21 | 0.99 | 83 | 0.268 | 0.030 | 0.97 | 0.14 | 3.3 |
| LOCK_6 cm_J105213+572650 | 23.7 | 20.4 | 16.8 | 0.07 | −0.07 | 0.02 | 57.99 | 0.99 | | <0.115 | | <0.79 | | |
| LOCK_6 cm_J105216+573529 | 18.7 | 17.5 | 15.1 | 0.20 | −0.20 | 0.00 | 287.12 | 0.99 | 85 | 0.206 | 0.040 | 1.39 | 0.32 | 4.0 |
| LOCK_6 cm_J105225+573322 | 21.3 | 18.6 | 15.7 | 0.64 | −0.64 | −0.02 | 231.92 | 0.99 | 89 | 4.515 | 0.160 | 0.81 | 0.03 | 0.5 |
| LOCK_6 cm_J105226+573711 | 24.8 | 23.4 | | 2.18 | 1.97 | −0.92 | 0.02 | 0.09 | | <0.167 | | <1.21 | | |
| LOCK_6 cm_J105227+573832 | 24.2 | 22.6 | | 1.79 | −1.74 | 0.42 | 0.31 | 0.60 | | <0.182 | | <1.00 | | |
| LOCK_6 cm_J105229+573334 | 25.1 | 24.1 | >20.2 | 1.68 | −1.64 | 0.33 | 0.04 | 0.15 | | <0.137 | | <0.98 | | |
| LOCK_6 cm_J105231+573027 | 22.1 | 19.1 | 16.0 | 1.00 | −0.60 | 0.80 | 64.56 | 0.99 | | <0.121 | | <0.62 | | |
| LOCK_6 cm_J105231+573204 | 22.2 | 20.1 | 17.2 | 2.28 | −0.03 | 2.28 | 0.68 | 0.48 | | <0.128 | | <1.15 | | |
| | 23.6 | 22.2 | 20.1 | 1.64 | 1.64 | −0.05 | 0.53 | 0.37 | | <0.128 | | <1.15 | | |
| LOCK_6 cm_J105231+573501 | 21.4 | 19.0 | 17.8 | 0.76 | −0.44 | −0.63 | 94.10 | 0.99 | 95 | 0.203 | 0.040 | 0.59 | 0.19 | 3.4 |
| | 21.2 | 18.9 | 17.5 | 2.68 | 2.68 | −0.03 | 0.26 | 0.00 | 95 | 0.203 | 0.040 | 0.59 | 0.19 | 3.4 |
| LOCK_6 cm_J105233+573057 | 20.2 | 18.5 | 16.0 | 0.89 | −0.87 | −0.17 | 144.83 | 0.99 | | <0.124 | | <−0.48 | | |
| LOCK_6 cm_J105234+572643 | 21.8 | 20.3 | 18.1 | 0.43 | −0.34 | 0.27 | 47.11 | 0.99 | | <0.116 | | <0.75 | | |
| LOCK_6 cm_J105235+572640 | 21.3 | 19.7 | 17.0 | 1.85 | 1.65 | −0.84 | 7.96 | 0.98 | | <0.116 | | <0.75 | | |
| LOCK_6 cm_J105237+572147 | 21.8 | 20.0 | 17.2 | 1.26 | −0.61 | −1.11 | 17.86 | 0.99 | | <0.116 | | <0.63 | | |
| LOCK_6 cm_J105237+573104T | 21.8 | 19.0 | 16.0 | 0.23 | 0.10 | 0.20 | 203.41 | 0.99 | 99* | 59.452 | 1.910 | 1.00 | 0.03 | 4.1 |
| LOCK_6 cm_J105238+572221 | >25.5 | >24.5 | | | | | | | | <0.115 | | <0.76 | | |
| LOCK_6 cm_J105238+573321 | 22.4 | 20.3 | 17.5 | 1.78 | −1.48 | −1.00 | 2.38 | 0.92 | | <0.138 | | <0.97 | | |
| LOCK_6 cm_J105239+572430 | 17.8 | 17.2 | 16.0 | 1.12 | −0.84 | −0.73 | 237.62 | 0.99 | 100 | 0.144 | 0.030 | 0.92 | 0.22 | 1.3 |
| LOCK_6 cm_J105241+572320 | 23.3 | 20.9 | 17.5 | 0.13 | 0.00 | −0.13 | 29.55 | 0.99 | 101 | 1.724 | 0.070 | 0.59 | 0.04 | 0.8 |

[a] Magnitudes in all bands are Vega magnitudes.

[b] For this source the $V$ magnitude is not available due to a problem with the electronic readout in the CCD.

**Table 3.** continued.

| NAME | $V^a$ | $I^a$ | $K'^a$ | Δ (″) | ΔRA (″) | ΔDec (″) | $LR$ | Rel. | 20 cm Nr. | $F20$ mJy | $F20_{\rm err}$ | $\alpha_{\rm r}$ | $\alpha_{\rm r\ err}$ | Δ6−20 (″) |
|---|---|---|---|---|---|---|---|---|---|---|---|---|---|---|
| LOCK_6 cm_J105242+571915 | 18.0 | 16.7 | 14.7 | 1.10 | −0.20 | 1.08 | 297.78 | 0.99 | 103 | 0.246 | 0.030 | 0.35 | 0.17 | 1.2 |
| LOCK_6 cm_J105245+573615 | 21.8 | 19.2 | | 0.61 | 0.33 | −0.52 | 135.25 | 0.99 | 104 | 0.458 | 0.060 | 0.46 | 0.12 | 2.8 |
| LOCK_6 cm_J105249+573626 | 25.8 | 22.0 | 18.9 | 0.27 | 0.27 | −0.02 | 6.94 | 0.97 | | <0.170 | | <1.00 | | |
| LOCK_6 cm_J105252+572859 | 17.8 | 16.5 | 14.2 | 0.17 | −0.17 | 0.03 | 797.05 | 0.99 | 105 | 0.202 | 0.030 | 0.61 | 0.17 | 3.4 |
| LOCK_6 cm_J105254+572341 | 23.1 | 20.8 | 18.2 | 0.67 | −0.34 | −0.58 | 16.99 | 0.99 | | <0.115 | | <−0.06 | | |
| LOCK_6 cm_J105255+571950 | 24.4 | 22.6 | 18.1 | 0.53 | −0.51 | −0.14 | 6.65 | 0.97 | 109 | 2.692 | 0.090 | 0.93 | 0.03 | 0.9 |
| LOCK_6 cm_J105259+573226 | >25.5 | 24.6 | 20.1 | 0.33 | 0.30 | 0.13 | 0.00 | 0.00 | 113 | 0.285 | 0.040 | 0.38 | 0.13 | 2.4 |
| LOCK_6 cm_J105301+572521 | 22.9 | 20.0 | 17.2 | 0.08 | 0.00 | 0.08 | 92.84 | 0.99 | 114 | 0.151 | 0.030 | 0.38 | 0.19 | 0.5 |
| LOCK_6 cm_J105301+573333 | 21.8 | 19.2 | 16.3 | 1.22 | 1.21 | −0.14 | 43.30 | 0.99 | | <0.152 | | <0.97 | | |
| LOCK_6 cm_J105303+573429 | 25.8 | 23.3 | 18.5 | 0.92 | 0.80 | −0.45 | 0.47 | 0.70 | | <0.161 | | <0.74 | | |
| LOCK_6 cm_J105303+573526 | 21.8 | 19.8 | 17.1 | 0.93 | −0.10 | −0.92 | 34.49 | 0.99 | | <0.160 | | <0.71 | | |
| LOCK_6 cm_J105303+573532 | 22.0 | 20.3 | 17.1 | 0.70 | 0.64 | 0.30 | 30.62 | 0.99 | 116 | 0.366 | 0.040 | 0.81 | 0.18 | 1.0 |
| LOCK_6 cm_J105304+573055 | 22.2 | 19.0 | 15.8 | 0.44 | −0.44 | −0.03 | 167.26 | 0.99 | 119 | 0.440 | 0.040 | 0.69 | 0.10 | 0.3 |
| LOCK_6 cm_J105308+572223 | 20.8 | 18.7 | | 0.10 | −0.10 | 0.00 | 364.69 | 0.99 | 121 | 0.340 | 0.030 | 0.61 | 0.10 | 0.3 |
| LOCK_6 cm_J105308+573436 | 20.8 | 18.9 | 16.5 | 0.48 | −0.20 | −0.44 | 151.27 | 0.99 | | <0.166 | | <0.73 | | |
| LOCK_6 cm_J105310+573434 | 22.9 | 21.9 | 19.2 | 1.89 | −0.94 | −1.64 | 0.27 | 0.47 | | <0.167 | | <0.75 | | |
| | 23.2 | 21.7 | 19.6 | 2.16 | 1.71 | 1.33 | 0.10 | 0.18 | | <0.167 | | <0.75 | | |
| LOCK_6 cm_J105312+573111 | 24.6 | 21.3 | 17.9 | 0.59 | −0.57 | −0.16 | 7.95 | 0.98 | 126 | 0.232 | 0.040 | 0.74 | 0.16 | 1.4 |
| LOCK_6 cm_J105313+572507 | 25.9 | 23.7 | 17.5 | 0.66 | −0.17 | −0.64 | 0.70 | 0.77 | | <0.124 | | <0.41 | | |
| | 24.7 | 23.0 | 18.0 | 2.48 | 1.28 | −2.13 | 0.01 | 0.01 | | <0.124 | | <0.41 | | |
| LOCK_6 cm_J105314+572448 | 23.3 | 20.4 | | 0.13 | 0.10 | −0.08 | 55.04 | 0.99 | | 0.124 | | <−0.14 | | |
| LOCK_6 cm_J105314+573020 | 24.3 | 22.8 | 18.8 | 0.99 | −0.94 | −0.30 | 2.08 | 0.88 | 127 | 0.292 | 0.040 | 0.62 | 0.15 | 2.4 |
| | 24.4 | 23.3 | 19.8 | 1.59 | −1.31 | 0.91 | 0.09 | 0.04 | 127 | 0.292 | 0.040 | 0.62 | 0.15 | 2.4 |
| LOCK_6 cm_J105316+573551 | 19.1 | 18.2 | 16.7 | 0.86 | −0.40 | 0.77 | 129.49 | 0.99 | 128 | 0.255 | 0.050 | 0.64 | 0.20 | 1.6 |
| LOCK_6 cm_J105317+572722 | 24.2 | 22.9 | >20.2 | 0.95 | −0.91 | −0.27 | 2.19 | 0.90 | | <0.132 | | <1.10 | | |
| LOCK_6 cm_J105322+573652 | 21.8 | 19.2 | 16.4 | 0.53 | −0.50 | −0.16 | 128.50 | 0.99 | | <0.202 | | <1.00 | | |
| LOCK_6 cm_J105325+572911 | 17.9 | 17.2 | 15.7 | 1.21 | −0.87 | 0.84 | 169.03 | 0.99 | 134 | 0.552 | 0.040 | 0.51 | 0.13 | 1.3 |
| LOCK_6 cm_J105327+573316 | 22.2 | 20.5 | 18.1 | 0.61 | −0.54 | −0.30 | 40.77 | 0.99 | | <0.173 | | <0.42 | | |
| LOCK_6 cm_J105328+573535 | 22.2 | 19.4 | 16.4 | 0.55 | −0.44 | 0.33 | 87.01 | 0.99 | | <0.196 | | <0.82 | | |
| LOCK_6 cm_J105335+572157 | 25.0 | 24.4 | | 2.06 | 0.24 | 2.05 | 0.00 | 0.00 | | <0.139 | | −0.01 | | |
| LOCK_6 cm_J105335+572921 | 23.3 | 20.0 | 17.0 | 0.46 | −0.34 | 0.31 | 71.86 | 0.99 | 138 | 0.214 | 0.040 | 0.53 | 0.18 | 1.4 |
| LOCK_6 cm_J105342+573026 | >25.5 | 23.9 | 20.1 | 0.95 | 0.27 | 0.91 | 0.24 | 0.55 | 142 | 0.274 | 0.040 | 1.08 | 0.20 | 1.2 |
| LOCK_6 cm_J105347+573349 | 22.6 | 22.3 | | 0.74 | −0.70 | 0.22 | 4.64 | 0.96 | | <0.203 | | <0.21 | | |
| LOCK_6 cm_J105348+573033 | 23.3 | 21.2 | 18.5 | 0.71 | −0.64 | 0.31 | 14.96 | 0.99 | | <0.180 | | <0.80 | | |

[a] Magnitudes in all bands are Vega magnitudes.

**Table 4.** Radio/X-ray associations.

| Radio source | $F_{6\ \mathrm{cm}}$ (mJy) | $\alpha_{\mathrm{r}}$ | $I$ | $K'$ | Nr. $X$ | $\Delta R-X$ ($''$) | $Fx^a$ | Type | $z$ | Log $L_{5\ \mathrm{GHz}}$ (W/Hz) |
|---|---|---|---|---|---|---|---|---|---|---|
| LOCK_6 cm_J105148+573248T | 5.03 | 0.95 | 21.4 | 18.0 | 12 | 0.8 | 0.72 | 2 | 0.990 | 25.41 |
| LOCK_6 cm_J105237+573104T | 16.45 | 1.00 | 19.0 | 16.0 | 116 | 3.5 | 0.57 | 2 | 0.708[b] | 25.56 |
| LOCK_6 cm_J105239+572430 | 0.06 | 0.59 | 17.2 | 16.0 | 32 | 0.8 | 7.02 | 1 | 1.113 | 23.61 |
| LOCK_6 cm_J105252+572859 | 0.10 | 0.41 | 16.5 | 14.2 | 901 | 1.2 | 0.12 | 2 | 0.204 | 22.07 |
| LOCK_6 cm_J105254+572341 | 0.13 | <−0.06 | 20.8 | 18.2 | 513 | 1.5 | 0.43 | 1 | 0.761 | 23.54 |
| LOCK_6 cm_J105303+573532 | 0.14 | 0.81 | 20.3 | 17.1 | 827 | 2.8 | 0.18 | 2 | 0.249 | 22.42 |
| LOCK_6 cm_J105316+573551 | 0.09 | 0.64 | 18.2 | 16.7 | 6 | 0.7 | 9.32 | 1 | 1.204 | 23.87 |
| LOCK_6 cm_J105328+573535 | 0.08 | <0.82 | 19.4 | 16.4 | 815 | 4.3 | 0.18 | 3 | 0.700[b] | 23.24 |
| LOCK_6 cm_J105348+573033 | 0.09 | <0.80 | 21.2 | 18.5 | 117 | 1.3 | 0.66 | 2 | 0.780 | 23.41 |
| *New radio/X-ray associations found with the XMM-Newton source list* | | | | | | | | | | |
| LOCK_6 cm_J105238+573321 | 0.05 | <0.97 | 20.3 | 17.5 | 52061 | 2.3 | 0.17 | 2 | 0.707[b] | 23.04 |
| LOCK_6 cm_J105255+571950 | 1.02 | 0.93 | 22.6 | 18.1 | 52149 | 1.8 | 0.07 | 2 | 1.450 | 25.13 |
| LOCK_6 cm_J105304+573055 | 0.18 | 0.69 | 19.0 | 15.8 | 52198 | 1.6 | 0.05 | 2 | 0.805 | 23.74 |
| LOCK_6 cm_J105347+573349 | 0.17 | <0.21 | 22.3 | | 52048 | 2.5 | 0.21 | 1 | 2.586 | 24.96 |

[a] Unit of $10^{-14}$ erg cm$^{-2}$ s$^{-1}$. Note: The ROSAT/X-ray data, including spectroscopic classification and redshift are all taken from Lehmann et al. (2001), except for the X-ray source 116 for which the references are Hasinger et al. (1998) and Lehmann et al. (2000). The XMM/X-ray data are from Lehmann et al. (2003), in preparation.

[b] The sources J105237+573104T and J105238+573321, although with the same redshift, are not members of the cluster at $z = 0.700$ associated with the radio source J105328+573535. However, these three radio/X-ray sources suggest the presence of an overdensity extending over at least a few Mpc at $z \sim 0.7$.

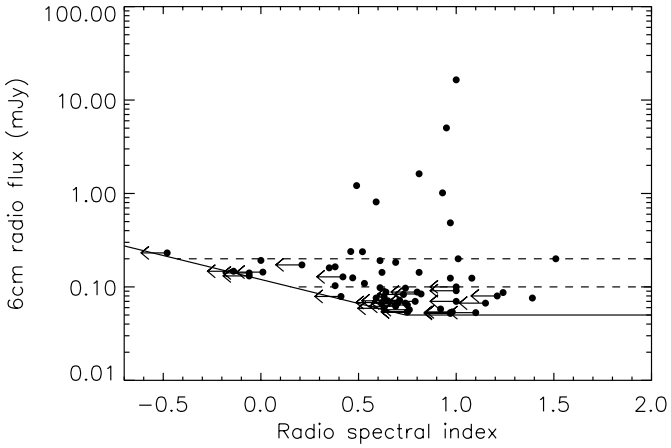


**Fig. 11.** The 6 cm flux as a function of the radio spectral index. The solid line shows the minimum value of the spectral index below which no 20 cm detection is possible due to the flux density limit of the 20 cm survey. The two dashed lines are at $S_{6\ \mathrm{cm}} = 0.1$ mJy and at $S_{6\ \mathrm{cm}} = 0.2$ mJy.

We first studied the dependence of the spectral index distribution on the 6 cm radio flux. However, because of the higher flux limit at 20 cm, if we consider all the 6 cm radio sources, the observed distribution of the spectral indices is a biased estimate of the true distribution. The main reason for this is that, given a minimum value for the 20 cm flux, for each value of the 6 cm flux there exists a minimum value of the spectral index below which no 20 cm detection is possible. In Fig. 11 we plot the 6 cm flux as a function of the spectral indices (or their upper limits). For illustrative purpose we show (solid line) the minimum spectral index, as a function of the 6 cm flux, for sources which could have been detected in the more sensitive, central part of the 20 cm image ($S_{\mathrm{lim}} = 0.120$ mJy). The two dashed lines in Fig. 11 are drawn at $S_{6\ \mathrm{cm}} = 0.1$ mJy and at $S_{6\ \mathrm{cm}} = 0.2$ mJy. As clearly shown in Fig. 11, below 0.1 mJy there is a bias against detection of sources with a radio spectral index flatter than ∼0.5. In fact, among the 32 sources with $S_{6\ \mathrm{cm}} < 0.10$ mJy, only 8 are detected at 20 cm. The situation is much better at $S_{6\ \mathrm{cm}} > 0.10$ mJy, where we have 31 sources with only 8 upper limits and a more relaxed bias (present only between 0.1 and 0.2 mJy, see Fig. 11) against flat spectra sources. We have therefore considered in this statistical analysis only sources with $S_{6\ \mathrm{cm}} \geq 0.10$ mJy.

These sources have been divided in two flux bins ($0.1 \leq S_{6\ \mathrm{cm}} < 0.2$ mJy and $S_{6\ \mathrm{cm}} > 0.20$ mJy, see dashed lines in Fig. 11) and for each bin we have computed, taking into account also the upper limits, the median spectral index $\alpha_{\mathrm{r\_med}}$, the mean of the spectral index distribution $< \alpha_{\mathrm{r}} >$ and the fraction of flat and inverted spectrum sources $f(\alpha_{\mathrm{r}} < 0.5)$. The results, reported in Table 5, suggest the presence of a flattening of the radio spectral index in the faint flux bin. The statistical significance of the difference between the spectral index distributions in the two flux interval bins has been tested using the statistical tests in the ASURV software package. All tests suggest that the two distributions are different with a confidence level of the order of 99.8% (corresponding to about 3 $\sigma$), with mean and median spectral index flattening from ∼0.75 for $S_{6\ \mathrm{cm}} \geq 0.2$ mJy to ∼0.35 for $0.1 \leq S_{6\ \mathrm{cm}} < 0.2$ mJy.

Also the fraction of flat spectrum sources appears to be different in the two flux intervals, changing from ∼25% for the brighter sample to ∼58% for the fainter sample.

Our results for the sources with $0.1 < S_{6\ \mathrm{cm}} \leq 0.2$ mJy are in excellent agreement with previous results in the same

**Table 5.** The radio spectral index versus 6 cm radio flux

| 4860 MHz Flux Interval (mJy) | Median $\alpha_{r\_med}$ | Mean $< \alpha_r >$ | $f(\alpha_r < 0.5)$ |
|---|---|---|---|
| $0.1 \leq S < 0.2$ | $0.37 \pm 0.10$ | $0.28 \pm 0.08$ | $11/19 \sim 58\%$ |
| $0.2 \leq S < 16.5$ | $0.81 \pm 0.14$ | $0.73 \pm 0.12$ | $3/12 \sim 25\%$ |

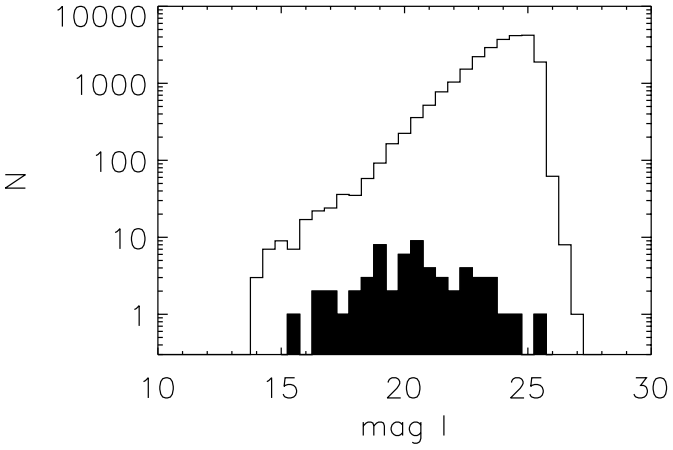


**Fig. 12.** Magnitude distributions for the $I$ band. The empty histogram shows the distribution of the whole optical sample, while the filled histogram shows the distribution of the optical counterparts of the 6 cm radio sources.

flux interval (Donnelly et al. 1987) and with those found at even fainter fluxes (Fomalont et al. 1991 for a sample selected at 5 GHz with $0.016 < S_{6\,\mathrm{cm}} \leq 0.2$ mJy; Richards et al. 1999 for a sample selected at 8.5 Ghz with $S_{\mathrm{med}} \sim 0.03$ mJy).

Vice versa, the suggestion from our data of a steeper average spectral index for $S_{6\,\mathrm{cm}} \geq 0.2$ mJy appears to be in contrast with the conclusion reached by Fomalont et al. (1991) and Windhorst et al. (1993). They found, in fact, that while the median spectral index reaches the maximum steepness in the 10–100 mJy range (see Fig. 5 in Windhorst et al. 1993), it decreases to ~0.4 below 1 mJy and remains constant over almost a factor of 100 in flux density down to the faintest observed level (~0.016 mJy). Both our sample and those listed by Fomalont et al. (see their Table 9) in the flux range $0.2 \leq S_{6\,\mathrm{cm}} \leq 2$ mJy are however very small; only much larger surveys at these fluxes could better determine at which flux the change in the spectral properties (from steep spectra at high flux to flat spectra at low flux) is actually occurring.

Finally we calculated the median of the spectral index distribution of the entire 6 cm sample with $S_{6\,\mathrm{cm}} \geq 0.1$ mJy. The median value of the 6 cm selected sample is $0.52 \pm 0.13$. This value is consistent with the general trend of a flattening of the mean radio spectral index with increasing selection frequency (Fomalont et al. 1991; Windhorst et al. 1993) and with the recent results of Richards (2000), who found that, while the average spectral index for the 1.4 GHz radio sample in the HDF is $0.85 \pm 0.2$, for the 8.5 GHz selected sample it is $0.4 \pm 0.1$. This flattening of the spectral distribution is consistent with the idea that high frequency samples preferentially select sources in which the radio emission is dominated by a flat-spectrum nuclear component (either a nuclear starburst with a free-free emission or a synchrotron self-absorbed AGN) and/or sources in which the radio emission is produced by thermal radio emission from large-scale star formation (Windhorst et al. 1993; Richards et al. 2000).

### 5.2. Magnitude distribution and colour-colour diagram

In absence of spectroscopic data, the magnitude and colour distributions of the optical counterparts can be used to derive some hints on the nature of faint radio sources. The $I$ magnitude distribution of the optical counterparts of the radio sources is shown as filled histogram in Fig. 12. The empty histogram shows the magnitude distribution of the whole data set over the region covered by the radio catalogue (a circle of 10′ radius). These counts are in good agreement with the source counts found in other surveys (Pozzetti et al. 1998). It is clear from Fig. 12 that the $I$ magnitude distribution of the optical counterparts of radio sources reaches a maximum at magnitudes ($I \sim 20$–$21$) well above our limiting magnitude, consistently with the fact that a large fraction of the radio sources is optically identified (see Sect. 4.2). A similar result has been obtained by Richards et al. (1999) in the identification of the microjansky radio sources in the Hubble Deep Field region. Eighty-four out of 111 radio sources have been identified down to $I = 25$ mag, with the bulk of the sample identified with relatively bright ($I \leq 22$ mag) galaxies.

In Fig. 13 we show the $V - I$ versus $I - K'$ colour for all the radio sources in the Lockman Hole with a magnitude measurement in all three bands (42 objects) or an upper limit either in $V$ or in $K'$ (4 objects; see symbols with arrows in the figure). Typical evolutionary tracks from $z = 0$ to $z = 2$, computed convolving the models' spectral energy distributions with the appropriate filters, are shown for elliptical galaxies (solid line: $\tau = 0.3$ IMF = Scalo age = 12.5 Gyrs; dot dashed line: $\tau = 1$) and late–type (Sab–Sbc) galaxies (dashed line: $\tau = 10$ age = 12.5 Gyrs; courtesy of L. Pozzetti).

This comparison between data and models suggests that all (or most of) the objects above the diagonal line (filled squares) are likely to be high redshift ($z \geq 0.5$) early–type, passively evolving galaxies. The other objects (empty squares) can be late–type, star–forming galaxies at all redshifts or early–type galaxies at low redshift ($z \leq 0.5$).

In the upper and right part of the figure we show objects for which no information in $V$ and $K'$ magnitudes, respectively, are available. This is due to the fact that the fraction of the radio data image covered by the $V$ and $K$ catalogues are ~95% and ~70%. These objects, shown as circles, are tentatively assigned a classification on the basis of the available colour (see figure caption).

### 5.3. Radio flux versus optical magnitude

Figure 14 shows the 6 cm radio flux versus the $I$ band magnitude for all the 63 radio sources ($I$ band upper limits are shown for the 5 radio sources with no optical counterpart). Superimposed are the lines corresponding to constant values

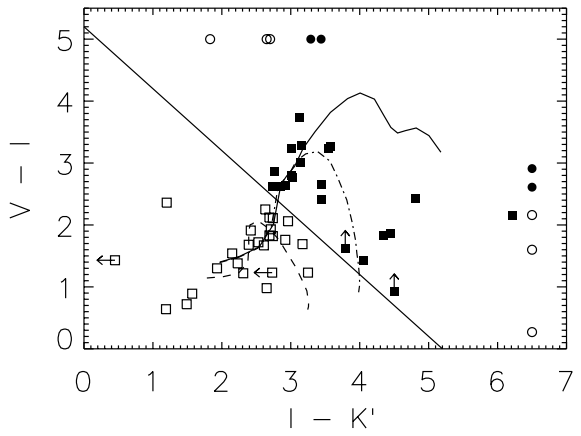


**Fig. 13.** $V - I$ versus $I - K'$ colour for all the radio sources in the Lockman Hole. The diagonal line represents $V-K = 5.2$. Typical evolutionary tracks from $z = 0$ to $z = 2$ are shown for early-type galaxies (solid line: $\tau = 0.3$ IMF = Scalo age = 12.5 Gyrs; dot dashed line : $\tau = 1$) and Sab Sbc galaxies (dashed line: $\tau = 10$ age = 12.5 Gyrs; courtesy of L. Pozzetti). Sources above the diagonal line are likely to be high redshift ($z \geq 0.5$) early-type galaxies and are plotted as filled squares. Sources below the diagonal line can be late-type, star forming galaxies at all redshifts or early-type galaxies at low redshift ($z \leq 0.5$) and are plotted as empty squares. In the upper and right part of the plot we show objects (plotted as circles) for which no information in $V$ and $K'$ magnitudes, respectively, are available. We tentatively assigned a classification on the basis of the available colour: filled circles are sources with $V-I > 2.5$ or $I-K' > 3.0$ (i.e. sources probably similar to the sources plotted as filled squares), open circles are sources with $V - I < 2.5$ or $I - K' < 3.0$.

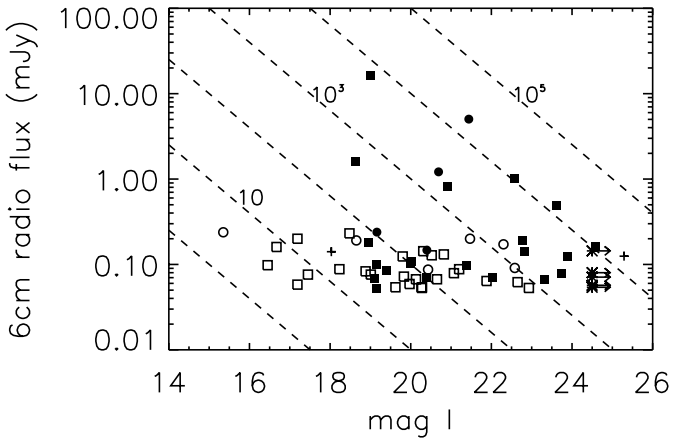


**Fig. 14.** The $I$ band magnitude versus the 6 cm radio flux for all the 63 radio sources. Symbols as in Fig. 13 except for the two crosses that show the objects for which only an $I$ band magnitude is available and the five arrows that show the radio sources without identification in the $V\,I$ and $K'$ band. The lines represent different radio to optical ratios $R$, corresponding to $R = 1, 10, 10^2, 10^3, 10^4, 10^5$.

for the observed radio-to-optical ratios $R$, defined as $R = S \times 10^{0.4(I-12.5)}$, where $S$ and $I$ are the radio flux in mJy and the apparent magnitude of sources respectively. The symbols are the same as those defined in the previous figure, except for the crosses, which represent the objects for which only an $I$ band magnitude is available and therefore were not shown in the colour–colour diagram.

This figure, although limited to a relatively narrow range of radio fluxes (see Fig. 8a in Kron et al. 1985 for a similar plot at higher flux level), shows that the two classes of objects defined on the basis of the colour–colour diagram have a different distribution in the radio flux–optical magnitude diagram. In particular, all the objects at large radio-to-optical ratios ($R \geq 1000$) have colours typical of passively evolving galaxies at relatively high redshift. On the basis of this plot we would conclude that also the five radio sources without optical identification are likely to belong to this class. No object of this class, instead, appears in this plot at low values of $R$ ($R \leq 30$), consistent with previous findings (see, for example, Gruppioni et al. 1999) that objects with these values of $R$ are mainly identified with star–forming galaxies. The situation is less well defined for intermediate values of $R$ ($30 < R < 1000$) where the two populations defined on the basis of Fig. 13 are not clearly separated in this plot. Only spectroscopic data can help in better defining the relative proportions of the two populations in this range of $R$. In any case, this analysis already allows us to conclude that at least about 50% of the radio sources in a 5 GHz selected sample with limiting flux $S_{6\ \mathrm{cm}} \geq 0.05$ mJy is associated to early–type galaxies. A similar conclusion was reached by Gruppioni et al. (1999) for a 1.4 GHz selected sample ($S_{21\ \mathrm{cm}} \geq 0.2$ mJy), for which a substantial fraction of spectroscopic identifications was available.

### 5.4. Extremely red radio galaxies

In Fig. 15 we show the $I - K'$ colour as a function of the radio flux, of the $I$ magnitude and of the radio-to-optical ratio $R$. While no obvious correlation is seen between $I - K'$ and radio flux, there appear to be significant correlations between $I - K'$ and both $I$ magnitude and radio-to-optical ratio $R$.

Both of them are significant at more than $5\sigma$ level on the basis of the Spearman rank test. A similar trend for the optically fainter radio sources to have redder $I - K$ colours was found by Richards et al. (1999) in their identification of fainter radio sources in the HDF and SSA13 fields. From Fig. 15 it is evident that almost all the counterparts of the radio sources in the magnitude range $22.5 < I < 24.5$ or with a radio-to-optical ratio greater than 1000 are red objects with $I - K' > 3$ and that a high fraction (6/10) of these faint objects can be classified as Extremely Red Objects (EROs) on the basis of a colour $I - K' > 4$ (McCarthy et al. 1992; Hu & Ridgway 1994). These EROs sources are not present at magnitudes I brighter than $I \sim 22.5$ mag and among sources with a radio-to-optical ratio lower than 1000.

The very red colours of EROs are well known to be consistent with both old passively evolving distant ($z > 0.8$) elliptical galaxies (e.g. Cohen et al. 1999; Spinrad et al. 1997) and dust–reddened starburst galaxies (e.g. Cimatti et al. 1998; Smail et al. 1999). The identification of the nature of EROs is an important test for models of galaxy formation and evolution and therefore the relative proportions of these two classes of objects among EROs has been lively debated in the last few years. However, because of the faintness of these objects in the optical bands, very few spectroscopic confirmations were

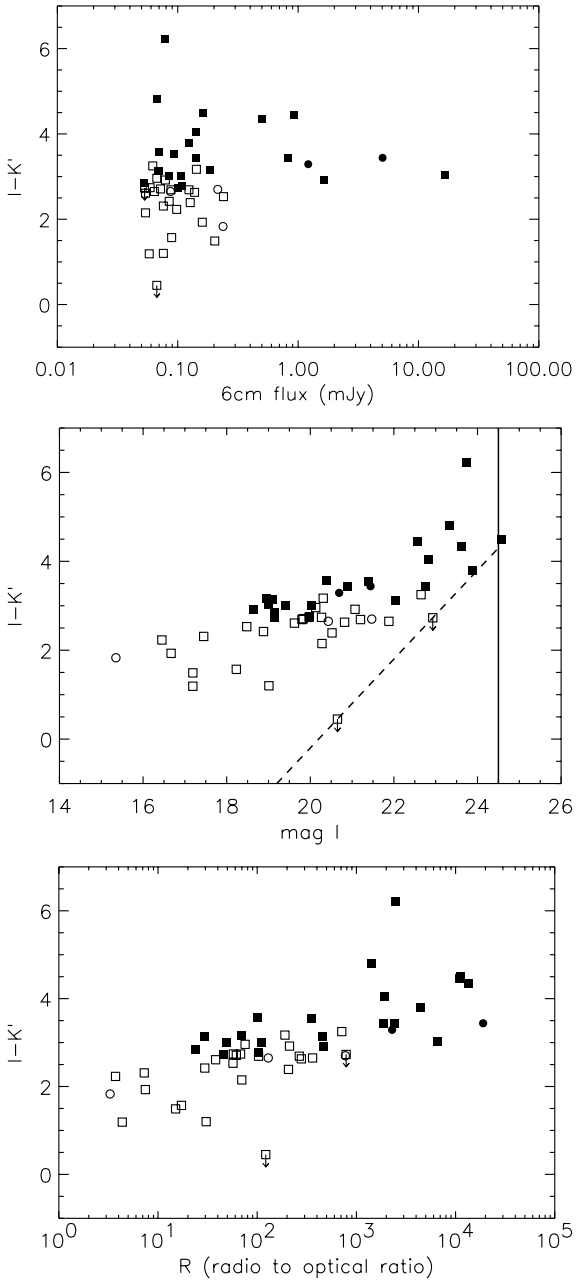


**Fig. 15.** The $I-K'$ colour as function of the total radio flux (top panel), of the $I$ band magnitude (central panel) and of the radio-to-optical ratio $R$ (bottom panel). Symbols as in Fig. 13. The vertical line in the central panel shows the magnitude limit $I = 24.5$ mag of our optical data while the dashed slanted line shows the $K' = 20.2$ mag limit. Sources within the two lines can not be detected due to the magnitude limits.

available until recently. Various authors, in absence of optical spectroscopy, used colour-colour diagrams and the overall spectral energy distribution to attempt to discriminate between passively evolving elliptical or dusty star–forming galaxies (Pozzetti & Mannucci 2000; Willott et al. 2001). Very recently, Cimatti et al. (2002), on the basis of extensive VLT spectroscopy of a complete sample of EROs with $K < 20$ have convincingly shown that the EROs population is indeed made up of both passively evolving elliptical and dusty star–forming galaxies and that the two classes of objects appear to be about equally populated and cover a similar redshift range ($0.7 < z < 1.5$). The average spectrum of the star–forming EROs suggests a substantial dust extinction with $E(B-V) \geq 0.5$.

Not yet having spectroscopic data for these radio–selected EROs, we here try to set some constraints on their nature using information from our own radio data and from existing ISO data. If these sources were dusty starbursts at $z \sim 1$, from the average dust extinction of $E(B-V) = 0.5$ suggested by Cimatti et al. (2002) for this class of objects we estimated $\Delta I \sim 2.7$ mag and $\Delta(I-K') \sim 1.9$ using the extinction law of Calzetti (1997) for objects at $z \sim 1$. A dust extinction of $E(B-V) = 0.5$ is in agreement with the extinction estimated by Willott et al. (2001) studying six extremely red sources ($R-K > 5.5$) from the 7C radio sample. From the fit of their spectral energy distribution they found six best-fit galaxy models with a dust extinction in the range $0.2 \leq E(B-V) \leq 0.8$.

Using the above extinction corrections the intrinsic colours and the radio to optical ratios of the 6 EROs here selected ($2.15 < I-K' < 4.32$ and $50 <$ radio to optical ratio $< 1200$) would become formally consistent with those typical of late type galaxies. However, under this assumption, their star formation rate (SFR) in massive stars, estimated from the radio emission using $\mathrm{SFR}(M \geq 5\ M_\odot) = L_{1.4}/(4.0 \times 10^{21}\ \mathrm{W\,Hz^{-1}})$ (Cram et al. 1998) and assuming $z \sim 1$, would be in the range 100–2300 $M_\odot\,\mathrm{yr}^{-1}$. Because of the well established correlation between SFR and far infrared emission ($\mathrm{SFR}(M \geq 5\ M_\odot) = L_{60_{\mu m}}/(5.1 \times 10^{23}\ \mathrm{W\,Hz^{-1}})$; Cram et al. 1998), and assuming the spectral energy distribution of M 82, these values of SFR would imply 15 $\mu$m fluxes in the range 3–70 mJy and 90 $\mu$m fluxes in the range 10–200 mJy. However ISO observations of this field show that none of the six radio selected EROs selected is detected at 90 $\mu$m down to a flux limit of ∼60 mJy (Rodighiero et al., in preparation) and only two of them (LOCK_6 cm_J105255+571950 and LOCK_6 cm_J105314+573020) are detected at 15 $\mu$m with a flux of 1.5 and 0.7 mJy respectively, with an upper limit of ∼0.30 mJy for the other four sources (Fadda et al. 2002; Fadda et al. in preparation).

From this comparison of optical, radio and ISO data we conclude that most of our radio–selected EROs sources are likely not to be associated with dusty starburst galaxies, but rather with early-type galaxies, hosting an Active Galactic Nucleus (AGN) responsible of the radio activity, although some contribution from the radio emission also from a nuclear starburst activity can not be excluded.

This conclusion is also in agreement with most of previous spectroscopic findings on the nature of extremely red radio sources. Laing et al. (1983) showed that the light from the reddest $z \sim 1$ radio galaxies in the 3CRR sample (3C65) is dominated by an old (∼4 Gyr) stellar population. Subsequently, two extremely red radio galaxies at $z \sim 1.5$ have been discovered in the follow up of the faint Leiden Berkeley Deep Survey (Dunlop et al. 1996; Dunlop 1999). Keck spectroscopy of these galaxies shows that also in this case their red colours are due to an old stellar population (≥3 Gyr) and not to reddening by dust. A similar result has been recently obtained by Willott et al. (2001) studying six extremely red sources ($R-K > 5.5$)

from the 7C radio sample. The only example so far of an extremely red object with $I - K > 4$ selected from a radio survey and identified with a dusty star–forming galaxy has been found by Afonso et al. (2001) studying optical counterparts of the radio sources from the Phoenix Deep Radio Survey (see also Waddington et al. (1999) for a similar dusty galaxy with $I_{814} - K = 2.0$ and a likely redshift of $z = 4.424$).

Finally, it is interesting to note that the six radio selected EROs represent only ∼2% of all the sources with $I - K' > 4$ present in the area covered by the $K'$ data (∼300 sources with $I - K' > 4$ over ∼220 arcmin$^2$). This fraction could approximately double if most of the five radio sources with no $I$ band counterpart also belong to the EROs class, as suggested by the observed trend between colour and $I$ magnitude (see Fig. 15). Assuming that their radio luminosity is due to AGN activity, the small fraction of radio detection suggests a relatively small AGN content in the optically/near-infrared selected EROs population. This result is qualitatively in agreement with what suggested by the recent deep X-ray surveys. In the Hubble Deep Field North Caltech area, only 4 of the 33 EROs in the field have a hard X-ray detection in the ∼220 ksec exposure with the Chandra satellite (Hornschemeier et al. 2001). However, it is well known that luminous radio sources have lifetimes much smaller than the age of the early galaxies hosting these AGNs (≥3–4 Gyr). Therefore, if individual radio sources have lifetimes of about $\sim 10^8$ years (Condon 1992), then the number of EROs undergoing radio activity during their life would be much higher than that observed.

## 6. Conclusion

We have used the VLA radio telescope to image at 6 cm a circular region (10 arcmin radius) to a 4.5 $\sigma$ limit of ∼50 $\mu$Jy in the Lockman Hole. The region is centered around the ROSAT ultra-deep *HRI* field. A complete sample of 63 radio sources has been obtained. The differential source counts are in good agreement with those obtained by other surveys, confirming that while the slope of the counts shows a flattening below a flux density of ∼1–3 mJy, there is no indication for a significant change in the slope in the 6 cm counts between ∼0.1 and 1 mJy.

The availability of a 20 cm survey down to ∼0.12 mJy in the same area (de Ruiter et al. 1997), gave us the opportunity to study the radio spectral index as function of the radio flux. Dividing our 6 cm sample in two subsamples with fluxes lower and greater than 0.2 mJy, we find a flattening of the radio spectral index and an increase of the population of flat spectra radio sources in the fainter flux bin. Several explanations for the observed flattening compared with sources detected at higher flux density level are possible, including an increasing number of synchrotron self-absorbed AGNs among the microjansky population, and/or a rising component of thermal radiation from active star formation.

Using the available optical images in $V$ and $I$ bands, we performed the optical identification of the radio sources using the Likelihood Ratio Analysis. We found a likely optical identification for 58 of the 63 radio sources. From the reliability associated to the likelihood analysis we estimate that at most four of the proposed identifications may be spurious and therefore the identification rate with the "correct" optical counterpart is in the range ∼86%–92%. Moreover, for a subsample of 51 radio sources we have data also in the $K'$ band. For this subsample we find $K'$ counterparts for 49 sources (96% of identifications). These high identification rates are consistent with the observed magnitude distribution of the optical counterparts, which appears to reach a maximum at magnitudes ($I \sim 20$–$21$) well above the limiting magnitude of our optical data.

A cross correlation between the radio catalogue and the ROSAT catalogue and the XMM-Newton source list (106 sources detected in the 0.5–2.0 keV band down to a flux limit of $3.8 \times 10^{-16}$ erg cm$^{-2}$ s$^{-1}$, Lehmann et al. 2002) gives 13 reliable radio/X-ray associations. The percentages of the radio/X-ray associations are ∼21 per cent of the radio sample and ∼12 per cent of the XMM/X-ray sample.

From an analysis of a colour–colour diagram ($V - I$ versus $I - K'$) we divided the optical counterparts in two classes. The objects in the first class are likely to be high redshift ($z \geq 0.5$) early–type, passively evolving galaxies, while the objects in the second class can be both late–type, star–forming galaxies at all redshifts and early–type galaxies at low redshift ($z \leq 0.5$). This separation in two classes appears to have a physical basis, related to different radio emission mechanisms, as further supported by the fact these two classes of objects have a quite different distribution in the radio flux–optical magnitude diagram. In particular, all the objects at large radio-to-optical ratios ($R \geq 1000$) have colours typical of passively evolving galaxies at relatively high redshift. On the basis of this plot we suggest that also the five radio sources without optical identification are likely to belong to this class. No object of this class, instead, appears in this plot at low values of $R$ ($R \leq 30$), consistent with previous findings (see, for example, Gruppioni et al. 1999) that objects with these values of $R$ are mainly identified with star–forming galaxies. From this analysis based on colours and the radio-to-optical ratios we conclude that at least 50% of the radio sources in a 5 GHz selected sample with limiting flux $S_{6\,\mathrm{cm}} \geq 0.05$ mJy is associated to early–type galaxies. A similar conclusion was reached by Gruppioni et al. (1999) for a 1.4 GHz selected sample ($S_{21\mathrm{cm}} \geq 0.2$ mJy), for which a substantial fraction of spectroscopic identifications was available.

Our data also show a significant correlation between $I - K'$ colour and both $I$ magnitude and radio-to-optical ratio $R$, with the redder galaxies being associated with optically fainter radio sources and with higher radio-to-optical ratio. In particular, almost all the counterparts of the radio sources in the magnitude range $22.5 < I < 24.5$ are red objects with $I - K' > 3$ and a high fraction (6/10) of these red objects are EROs with $I - K' > 4$. By combining our radio data with existing ISO data we conclude that most of our six radio–selected EROs sources are likely not to be associated with dusty starburst galaxies, but rather with early-type galaxies, hosting an AGN responsible of the radio activity.

The six radio selected EROs represent only ∼2% of the optically selected EROs present in the field. If their radio luminosity is indeed a sign of AGN activity, the small fraction of radio detections suggests that the optically/near-infrared selected EROs population contains a relatively small fraction of

active AGN, in agreement with what suggested by recent deep X-ray surveys (Hornschemeier et al. 2001).

The very high percentage of optical identifications and the availability of near infrared and deep X-ray data make this sample one of the best samples of radio selected sources available at $\mu$Jy flux density level and well suited to study in detail the nature of faint 6 cm radio sources. With this aim, we already obtained spectroscopic data for about one third of the radio sample, while a programme to obtain spectroscopic data for all the sources is ongoing. The results of the optical spectroscopic classification and a more detailed comparison with the XMM source list will be presented in a forthcoming paper.

*Acknowledgements.* This work was supported by the Italian Ministry for University and Research (MURST) under grant COFIN01 and by Italian Space Agency (ASI). We thank L. Pozzetti for providing us the evolutionary tracks of Fig. 13, D. Fadda and G. Rodighiero for providing us ISOCAM and ISOPHOT data before publication, and the referee R. A. Windhorst for useful comments. G.P.S. acknowledges support under DLR grant 50 OR 9908.

## References

Afonso, J., Mobasher, B., Chan, B., & Cram, L. 2001, ApJ, 559, 101
Altschuler, D. R. 1986, A&AS, 65, 267
Benn, C. R., Rowan-Robinson, M., McMahon, R. G., Broadhurst, T. J., & Lawrence, A. 1993, MNRAS, 263, 98
Calzetti, D. 1997, AJ, 113, 162
Cimatti, A., Daddi, E., Mignoli, M., et al. 2002, A&A, 381, L68
Cimatti, A., Andreani, P., Rottgering, H., & Tilanus, R. 1998, Nature, 392, 895
Cohen, J. G., Blandford, R., Hogg, D. W., Pahre, M. A., & Shopbell, P. L. 1999, ApJ, 512, 30
Condon, J. J. 1980, ApJ, 242, 894
Condon, J. J. 1992, ARA&A, 30, 575
Condon, J. J. 1997, PASP, 109, 166
Condon, J. J., Cotton, W. D., Greisen, E. W., et al. 1998, AJ, 115, 1693
Cram, L., Hopkins, A., Mobasher, B., & Rowan-Robinson, M. 1998, ApJ, 507, 155
de Ruiter, H. R., Zamorani, G., Parma, P., et al. 1997, A&A, 319, 7
Donnelly, R. H., Partridge, R. B., & Windhorst, R. A. 1987, ApJ, 321, 94
Dunlop, J. S. 1999, in The Most Distant Radio Galaxies, ed. P. N. Best, H. J. A. Röttgering, & M. D. Lehnert KNAW Colloq. (Dordrecht: Kluwer), 14
Dunlop, J. S., Peacock, J. A., Spinrad, H., et al. 1996, Nature, 381, 581
Fadda, D., Flores, H., Hasinger, G., et al. 2002, A&A, 384, 848
Feigelson, E. D., & Nelson, P. I. 1985, ApJ, 293, 192
Fomalont, E. B, Windhorst, R. A., Kristian, J. A., & Kellermann, K. I. 1991, AJ, 102, 1258
Fomalont, E. B., Kellermann, K. I., Richards, E. A., Windhorst, R. A., & Partridge, R. B. 1997, ApJ, 475, L5
Georgakakis, A., Mobasher, B., Cram, L., et al. 1999, MNRAS, 306, 708
Gruppioni, C., Zamorani, G., de Ruiter, H. R., et al. 1997, MNRAS, 286, 470
Gruppioni, C., Mignoli, M., & Zamorani, G. 1999, MNRAS, 304, 199
Hammer, F., Crampton, D., Lilly, S. J., Le Fevre, O., & Kenet, T. 1995, MNRAS, 276, 1085
Hasinger, G., Burg, R., Giacconi, R., et al. 1998, A&A, 329, 482
Hasinger, G., Altieri, B., Arnaud, M., et al. 2001, A&A, 365, L45
Hornschemeier, A. E., Brandt, W. N., Garmire, G. P., et al. 2001, ApJ, 554, 742
Hu, E. M., & Ridgway, S. E. 1994, AJ, 107, 1303
Isobe, T., Feigelson, E. D., & Nelson, P. I. 1986, ApJ, 306, 490
Kaiser, N., Wilson, G., & Luppino, G. 2001, ApJL, submitted [astro-ph/0003338]
Kron, R. G., Koo, D. C., & Windhorst, R. A. 1985, A&A, 146, 38
Laing, R. A., Riley, J. M., & Longair, M. S. 1983, MNRAS, 204, 151
Lehmann, I., Hasinger, G., Schmidt, M., et al. 2000, A&A, 354, 35
Lehmann, I., Hasinger, G., Schmidt, M., et al. 2001, A&A, 371, 833
Lehmann, I., Hasinger, G., Murray, S. S., & Schmidt, M. 2002, Proc. of X-ray at Sharp Focus: Chandra Science Symp. ASP Conf. Ser., ed. S. Vrtilek, E. M. Schlegel, & L. Kuhi, in press [astro-ph/0109172]
McCarthy, P. J., Persson, S. E., & West, S. C. 1992, ApJ, 386, 52
Oort, M. J. A., & Windhorst, R. A. 1985, A&A, 145, 405
Partridge, R. B., Hilldrup, K. C., & Ratner, M. J. 1986, ApJ, 308, 46
Perley, R. A. 1989, in Synthesis Imaging in Radio Astronomy, ed. R. A. Perley, F. R. Schwab, & A. H. Bridle (ASP, San Francisco), 259
Pozzetti, L., Madau, P., Zamorani, G., Ferguson, H. C., & Bruzual, A. G. 1998, MNRAS, 298, 1133
Pozzetti, L., & Mannucci, F. 2000, MNRAS, 317L, 17
Prandoni, I., Gregorini, L., Parma, P., et al. 2001, A&A, 369, 787
Richards, E. A. , Kellermann, K. I., Fomalont, E. B., Windhorst, R. A., & Partridge, R. B. 1998, AJ, 116, 1039
Richards, E. A., Fomalont, E. B., Kellermann, R. A., et al. 1999, ApJL, 526, 73
Schmidt, M., Hasinger, G., Gunn, J., et al. 1998, A&A, 329, 495
Smail, I., Ivison, R. J., Kneib, J. P., et al. 1999, MNRAS, 308, 1061
Spinrad, H., Dey, A., Stern, D., et al. 1997, 484, 581
Sutherland, W., & Saunders, W. 1992, MNRAS, 259, 413
Waddington, I., Windhorst, R. A., Cohen, S. H., et al. 1999, ApJ, 526, L77
Waddington, I., Windhorst, R. A., Dunlop, J. S., Koo, D. C., & Peacock, J. A. 2000, MNRAS, 317, 801
Willott, C. J., Rawlings, S., & Blundell, K. M. 2001, MNRAS, 324, 1
Wilson, G., Kaiser, N., Luppino, G., & Cowie, L. L. 2001, ApJ, 555, 572
Windhorst, R. A., van Heerde, G. M., & Katgert, P. 1984, A&AS, 58, 1
Windhorst, R. A., Miley, G. K., Owen, F. N., Kron, R. G., & Koo, D. C. 1985, ApJ, 289, 494
Windhorst, R. A., Mathis, D., & Neuschaefer, L. 1990, in Evolution of the Universe of Galaxies, ed. R. G. Kron, ASP Conf. Ser., 10, 389
Windhorst, R. A., Fomalont, E. B., Partridge, R. B., & Lowenthal, J. D. 1993, ApJ, 405, 498
Wrobel, J. M., & Krause, S. W. 1990, ApJ, 363, 11
Yun, M. S., Reddy, N. A., & Condon, J. J. 2001, ApJ, 554, 803